QCD IN HEAVY QUARK PRODUCTION AND DECAY

Jim Wiss*
University of Illinois
Urbana, IL 61801

ABSTRACT

I discuss how QCD is used to understand the physics of heavy quark production and decay dynamics. My discussion of production dynamics primarily concentrates on charm photoproduction data which is compared to perturbative QCD calculations which incorporate fragmentation effects. We begin our discussion of heavy quark decay by reviewing data on charm and beauty lifetimes. Present data on fully leptonic and semileptonic charm decay is then reviewed. Measurements of the hadronic weak current form factors are compared to the nonperturbative QCD-based predictions of Lattice Gauge Theories. We next discuss polarization phenomena present in charmed baryon decay. Heavy Quark Effective Theory predicts that the daughter baryon will recoil from the charmed parent with nearly 100% left-handed polarization, which is in excellent agreement with present data. We conclude by discussing nonleptonic charm decay which are traditionally analyzed in a factorization framework applicable to two-body and quasi-two-body nonleptonic decays. This discussion emphasizes the important role of final state interactions in influencing both the observed decay width of various two-body final states as well as modifying the interference between interfering resonance channels which contribute to specific multibody decays.

*Supported by DOE Contract DE-FG0201ER40677.

1 Introduction

A vast amount of important data on heavy quark production and decay exists for both the beauty and charm sector—far more than I could possibly cover in two lectures. For this reason, most of my talk will cover the production of charm in fixed target experiments with an emphasis on my own experiment—E687.*

Charmed mesons were discovered by the Mark I Collaboration which studied the e^+e^- annihilation process at SLAC about 21 years ago.[2] In the intervening years, a large number of collider as well as fixed-target experiments have heavily mined the field of heavy quark physics. The discovery paper by the Mark I group reported on the observation of $\approx$ 230 fully reconstructed decays of the D^o into the $K^{\mp}\pi^{\pm}$ and $K^{\mp}\pi^{\pm}\pi^{+}\pi^{-}$ final state. Recent experiments are capable of amassing clean, fully reconstructed charm data decays which are in excess of 100,000 events. Millions of fully reconstructed events are anticipated for several experiments presently taking data.

1.1 Charm and QCD

Charm provides a rich QCD phenomenology in both the perturbative and nonperturbative regimes. Studies of production dynamics test leading order (LO) and next-to-leading order (NLO) perturbative QCD. Charm lifetime measurements test models based on $1/M_Q$ QCD expansions. Heavy Quark Effective Theory (HQET) predicts a large degree of daughter baryon polarization in both semileptonic and two-body nonleptonic decay. Semileptonic form factors test nonperturbative QCD methods such as Lattice Gauge Theories (LGT). Finally, exclusive hadronic decay measurements test factorization models based on QCD renormalization group methods. Exclusive charm hadronic decays underscore the importance of final state interactions which should be important in unravelling the pattern of CP violations in the b sector.

While discussing the physics contained in the above topics and illustrating it with real data, I would like to give you some feeling on how measurements are actually made. You will probably find that these lectures tilt too much in the direction of fixed-target experiments. Perhaps they serve as a sort of swan song since the future of fixed-target charm experiments in the United States is very short.

*A general description of E687 can be found in Ref. 1.

1.2 Charm Mesons

Figure 1 is a crude sketch of the spectrum and properties of the low-lying D (pseudoscalar) and D^* (vector) mesons which consist of a charm quark and an up, down, or strange antiquark. There are a large number of baryon and higher excited mesons and baryons as well which are not shown. Several of the most

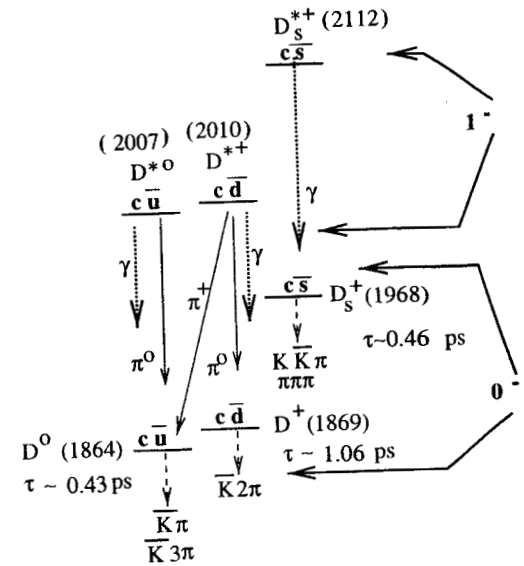

Fig. 1. Sketch of the spectrum of low lying charm mesons. The D^o amd D^+ mesons form a nearly degenerate strong isodoublet. The D_s^+ is shifted upwards by roughly 100 MeV. This mass splitting pattern is repeated for the D^*'s. Weak decays are shown by dashed arrows. Some strong and electromagnetic de-excitations of the D^* system into the ground state D system are shown by solid and dashed arrows. The approximate lifetimes of the ground state D system are indicated on the figure.

experimentally useful weak decay modes are shown in the figure. These are CKM-allowed decays where the charm quark is transformed to a strange quark resulting in a single kaon final state for the D^o and D^+, and a double kaon final state for the D_s^+. The D mesons have lifetimes ranging from about 1/2 to 1 psec. In a fixed-target experiment, a D^+ might typically be produced with a typical lab momenta of 100 GeV and will travel several centimeters before decaying. A high-quality vertex detector, such as a silicon microstrip detector, can readily measure a several centimeter decay path and thus cleanly tag a charm decay through its short but finite lifetime.

Perhaps the second best way of tagging charm particles is through the decay $D^{*+} \to \pi^+ D^o$ where the D^o decays into an easily reconstructible, all-charged decay mode such as the $K^{\mp}\pi^{\pm}$ final state. Owing to the small energy release in the decay $D^{*+} \to \underline{\pi}^+ D^o$, the soft (underlined) pion will carry only a small fraction of the lab momentum of the D and therefore can be very well-measured by a magnetic spectrometer. Most of the experimental smearing in reconstructing the D^{*+} mass is due to the D^o reconstruction which cancels in the mass difference $\Delta M \equiv M(D^o\pi^+) - M(D^o)$. This cancellation often results in a mass difference which is about ten times better resolved than the mass of the D^{*o}. By cutting on both $M(D^o)$ and ΔM, one can often get charm signals nearly as clean as those obtainable using lifetime tagging but without the technological inconvenience of having to build an expensive vertex tagging system. One can even extend the ΔM technique to tag semileptonic final states with a missing neutrino. Most of the data discussed in these lectures use either lifetime tagging or the $D^* \to D$ tagging trick to isolate and study charm.

2 The Physics of Charm Photoproduction

Charm photoproduction provides several nice illustrations of the successes and complications of applying perturbative QCD to production dynamics. We will begin on the most inclusive level by considering the center-of-mass energy dependence of the photoproduction cross section for charmed quarks. In order to delve deeper into the photoproduction process and study, *e.g.*, the P_t and X_f dependence for specific charm mesons, one must understand the hadronization process which describes the soft processes by which charmed quarks appear as charmed mesons and baryons. Studies of the kinematic dependence of photo- and hadroproduced charm-$\overline{\text{charm}}$ asymmetries provide surprisingly sensitive probes of QCD-inspired models of charm hadronization.

2.1 The Charm Quark Photoproduction Cross Section

At lowest order, and at energies significantly above charm threshold, the photoproduction of charmed quarks thought to be dominated by the photon-gluon fusion process is illustrated in lowest order by Fig. 2. The photon-gluon fusion

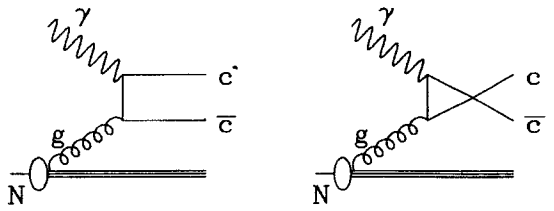

Fig. 2. Illustration of the lowest order contribution to the photon gluon fusion process. A gluon constituent of the nucleon interacts with a real photon to produce a $c\bar{c}$ pair. These graphs are both $\mathcal{O}(\alpha_{em}\alpha_s)$.

process is analogous to the pair production process $\gamma\mathcal{N} \to e^+e^-\,\mathcal{N}$, where a projectile photon interacts with a virtual photon from the nucleus to form an e^+e^- pair. Charm hadroproduction is thought to occur by a very similar process where a gluon from the projectile fuses with a gluon from target to form a $c\bar{c}$ pair.

The charm quark photoproduced cross section will depend linearly on the gluon density within the nucleon as well as the partonic cross section evaluated at the squared energy in the photon-gluon rest frame:

$$\sigma(\gamma p \to c\bar{c}) = \int_{4m_c^2/s}^{1} dx_g\; g(x_g,\mu^2)\;\; \hat{\sigma}(s\,x_g) \quad , \quad \hat{s} = s\,x_g. \tag{1}$$

The variable of integration, x_g, represents the fraction of the nucleon momentum carried by the incident gluon. The lower limit of integration is due to the fact that $\hat{s} \equiv s\,x_g$; the squared center-of-mass energy in the photon-gluon rest frame must exceed $(2m_c)^2$. The lowest order PGF cross section will grow slowly with increasing $\hat{s}$ due to the contributions of increasingly softer (lower x_f) gluons.

At next-to-leading order (NLO), the graphs of Fig. 2 are joined by the $\mathcal{O}(\alpha_{em}\,\alpha_s^2)$ contributions which were recently calculated by Frixione, Mangano, Nason, and Ridolfi[3] (FMNR). The NLO graphs (Fig. 3) include contributions with extra

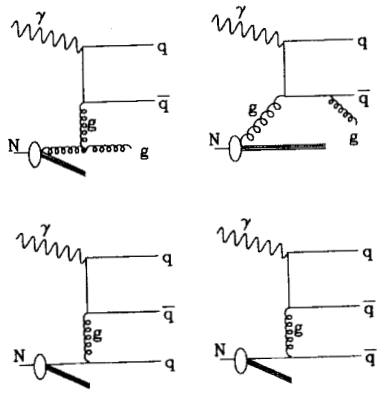

Fig. 3. NLO contributions to photon-gluon fusion which produce an additional gluon or quark in the final state.

quarks or gluons in the final state. Figure 4 compares the experimentally measured charm quark cross section to the FMNR predictions for several choices of renormalization scales, and gluon momentum distributions. The data are a reasonably good match to these predictions over a large kinematic range covering both fixed-target photoproduction experiments as well as the very recent data[4] on virtual photoproduction* of charm from HERA. The threshold condition $sx_g > 4\ m_c^2$ implies that the HERA data probes gluon density at fairly low x_g ($x_g > 1.6 \times 10^{-4}$) while fixed-target experiments typically probe in the more moderate x_g range ($x_g > 0.04$). Although the HERA charm event samples are fairly modest,† they carry an enormous kinematic lever arm which can be used to ultimately constrain parameters in the NLO description.

An apparent advantage of testing the QCD photoproduction model through the measurement of the $c\bar{c}$ cross-section energy dependence is that the theoretical cross section does not depend explicitly on a hadronization model, since ultimately the photoproduced quarks must somehow appear as charmed particles. Although some very nice models for hadronization exist (which we will discuss in Sec. 2.4),

*HERA defines the virtual photoproduction kinematic regime as $Q^2 < 4\ GeV^2$.

†For example, the ZEUS charm cross sections were based on 48 reconstructed $D^{*+} \to D^o\pi^+ \to (K^-\pi^+)\pi^+$ events.

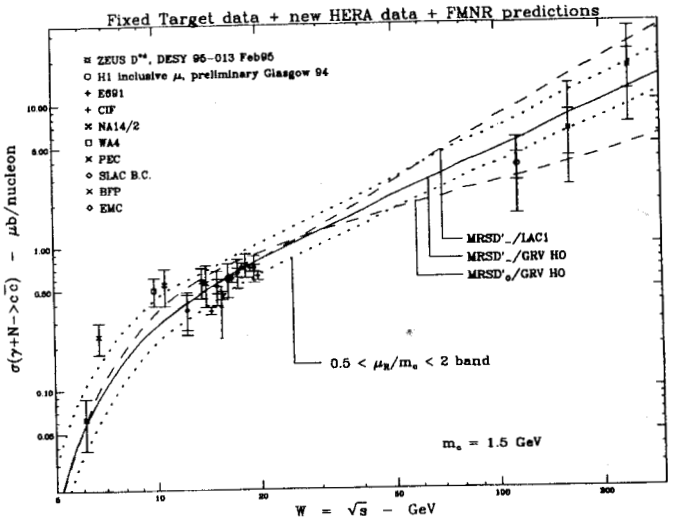

Fig. 4. Measured charm quark photoproduction cross sections compared to the FMNR NLO predictions for various gluon distribution parameterizations and renormalization scales.

they are phenomenological in the sense that although based on a general QCD-inspired framework, they parameterize many soft processes using inputs from experimental data.

Although hadronization assumptions may not enter directly into the predictions, they are required to experimentally measure the $c\bar{c}$ cross section. An experimenter will measure the yield of several different charm particles over a certain kinematic range where the experiment has a reasonably large, momentum-dependent reconstruction efficiency. To get a total $c\bar{c}$ cross section from such data, the experimenter must rely on a fragmentation model to know what fraction of the total charm cross section hadronizes into the final states being reconstructed. In addition, the hadronization model can affect the acceptance by controlling the fraction of charm particles with, *e.g.*, momenta outside of kinematic ranges of reasonable acceptance, or changing the overall reconstruction efficiency by affecting the multiplicity of particles which accompany the charm particle of interest.‡

‡This is an especially important effect in photoproduction where charm particles are tagged through the separation between a downstream (secondary) vertex containing the charm particle decay products and an upstream (primary) vertex which contains many of particles created through the hadronization process.

2.2 Nonperturbative Effects

In order to probe more deeply into charm photoproduction dynamics, one needs to consider the myriad of nonperturbative, soft-physics effects illustrated in Fig. 5. Fragmentation effects can change the direction of the charmed mesons relative to

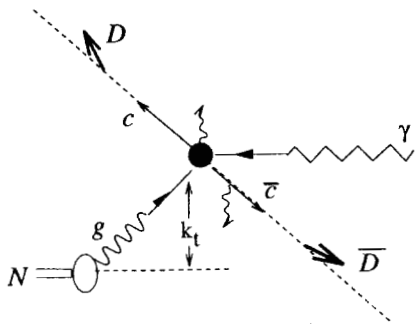

Figure 5: A cartoon of photoproduction of charm in the real world which illustrates several nonperturbative effects. The incident gluon can be thought to carry a small momentum component transverse to the incident nucleon called k_t. Soft gluon emission can accompany the charmed quark as it dresses, creating additional sources of relative $P_\perp$. A significant amount of quark energy is lost to the emerging D's while they hadronize.

the charmed quarks as well as significantly degrade their energy. A convenient variable to describe the energy fraction is called X_F for "Feynman X" which gives the fraction of available longitudinal momentum in the overall center of mass carried by an object divided by the maximum possible longitudinal momentum possible in that frame or:

$$X_F = \frac{2P_\parallel}{\sqrt{s}}. \qquad (2)$$

In a fixed-target experiment, X_F is approximately the fraction of the beam energy which appears in the charmed object.

Figure 6 compares the X_F distribution of charmed quarks and charmed mesons according to the JETSET-PYTHIA[6] string fragmentation model. Figure 6 shows that although each member of the $c\bar{c}$ pair carries an average of half of the incident beam energy, after fragmentation each charmed particle carries only about a quarter of the incident beam energy.

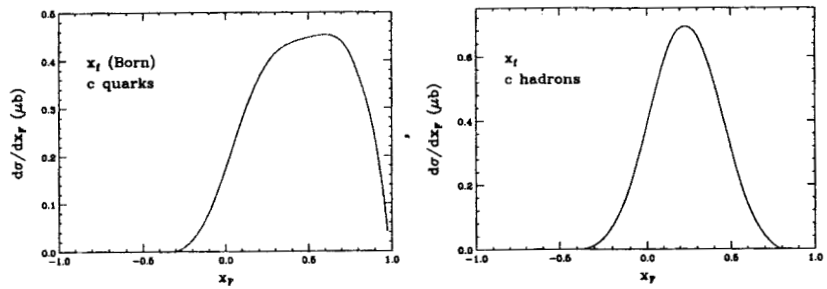

Figure 6: Comparison of the X_F distribution of charmed quarks (left) and charmed mesons (right) in LO photon-gluon fusion in the LO JETSET-PYTHIA model.

Figure 7 illustrates the importance of fragmentation effects by comparing the observed P_t^2 for photoproduced D^+ to the NLO FMNR predictions for charmed quarks (without fragmentation). The P_t^2 distribution of the data tracks fairly well with the PYTHIA MC which embeds LO PGF with LUND string fragmentation. The data clearly does not match the high end tail of the FMNR predictions for bare, charmed quarks where hard gluon emission is included in the NLO description. It is possible to match the P_t^2 spectrum of the data as shown in Fig. 8 by supplementing the NLO calculations with fragmentation effects such as intrinsic gluon k_t and momentum loss described by Peterson[5] fragmentation.

2.3 Correlations in Photoproduced $D\overline{D}$ Pairs

It is possible to fully reconstruct both members of a photoproduced $D\overline{D}$ pair in order to more fully probe photoproduction dynamics. As Fig. 9 shows, there are two ways of doing this. One can fully reconstruct both particles by detecting all of the decay products of both decays. Of course, one will necessarily pay a big price in statistics in acceptance and branching ratios to acquire a fully reconstructed double-D signal. Alternatively, one can kinematically tag the soft (underlined) pion from the decay $D^{*+} \to \underline{\pi}^+ D^o$ by exploiting charge and kinematic correla-

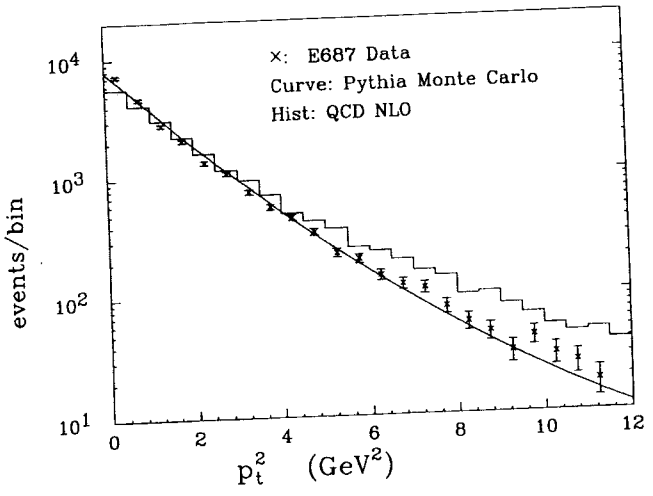

Figure 7: Overlay of the P_t^2 distribution for reconstructed D^+ mesons collected by E687 (with error bars) with the FMNR NLO predictions (histogram) and the PYTHIA Monte Carlo.

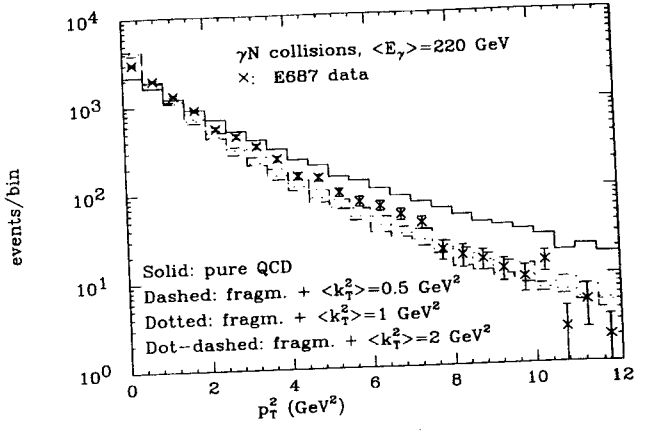

Figure 8: NLO calculations for various k_t and fragmentation options compared to E687 D^+ data. The Peterson fragmentation recipe is used which softens the momentum of the D^+ in the photon-gluon rest frame by a factor Z which is drawn from a QCD-inspired distribution. Fragmentation tends to soften the P_t^2 spectrum while k_t hardens this spectrum.

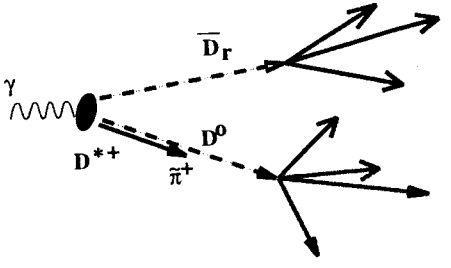

Figure 9: Two ways of studying photoproduced $D\overline{D}$ pairs. One can fully reconstruct both charmed particles. Alternatively, one can use a partially reconstructed double-D sample obtained by identifying the soft pion from $D^{*+} \to D^o\pi^+$ decay through the use of kinematic and charge correlation tagging.

tions between the pion and a fully reconstructed recoil $\overline{D_r}$. Because of the small energy release in $D^{*+} \to D^o\pi^+$, the soft pion, D^o, and D^{*+} all have approximately the same laboratory velocity. This allows one to estimate the momentum of a D^{*+} from just the soft pion by multiplying its momentum by the D^*/π mass ratio.§ The charge of the soft pion is correlated with the charm of the fully reconstructed, recoil D state, and the scaled pion momentum should approximately balance P_t with the recoil $\overline{D_r}$. We use the P_t balance variable $\Delta_t^2 = \mid 13.8\ \vec{P}_t(\pi^+) + \vec{P}_t(\overline{D_r}) \mid^2$. Figure 10 shows the signals for the fully reconstructed and partially reconstructed $D\overline{D}$ samples[7] which start with a baseline sample of $\approx 45,000$ inclusive D's reconstructed in the $K^{\mp}\pi^{\pm}$, $K^{\mp}\pi^{\pm}\pi^{\pm}$, and $K^{\mp}\pi^{\pm}\pi^{+}\pi^{-}$ final states.

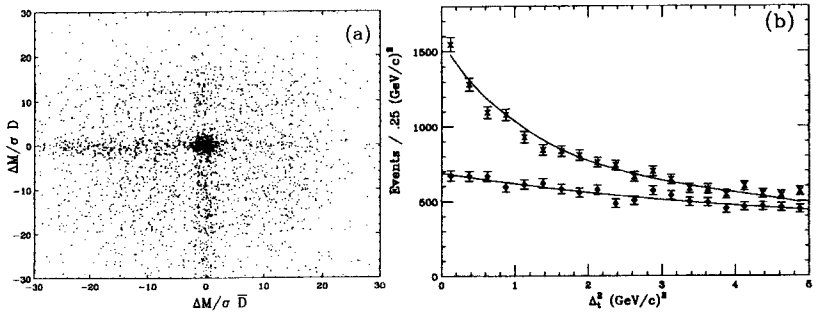

Fig. 10. (a) Scatter plot of the normalized mass of detached D candidates vs the normalized mass of the recoil $\overline{D}$ candidate. The normalized mass is the difference between the reconstructed and known D mass divided by the calculated event-by-event resolution. The accumulation near the origin consists of $\approx$ 320 fully reconstructed $D\overline{D}$ pairs. (b) Distribution of the P_t balance variable Δ_t^2 for right-sign and wrong-sign decay pion candidates. The upper curve is the form expected by fitting the net P_t^2 of fully reconstructed $D\overline{D}$ candidates and smearing slightly for errors due to reconstructing the P_t of the parent D^{*+} by scaling the P_t of the decay π^+. The right-sign excess below $\Delta_t^2 = 4\ GeV^2$ consists of $\approx$ 4530 events.

We have explored the kinematical correlations of the $D\overline{D}$ pair using several longitudinal and transverse variables. The acoplanarity angle, $\Delta\phi$, which is illustrated by Fig. 11, is used by many experimental groups since most experiments have excellent acceptance and resolution in this variable. A related variable is the net transverse momentum of the observed $D\overline{D}$ pair or $P_t^2(D\overline{D}) = |\vec{P}_t(D) + \vec{P}_t(\overline{D})|^2$.

§To take into account the very slight soft pion kinetic energy in the D^* rest frame, we actually use a scaling factor of 13.8 which is slightly smaller than the D^{*+}/π^+ mass ratio.

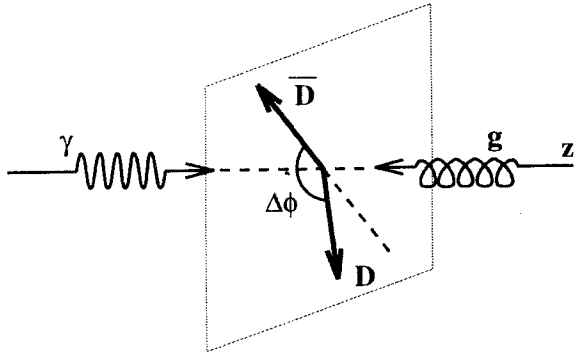

Fig. 11. The acoplanarity angle $\Delta\phi$ is the angle between the D and $\overline{D}$ in a plane transverse to the collision axis. If k_t or final-state gluon emission were negligible, the $\Delta\phi$ distribution would peak sharply at π radians.

A good longitudinal correlation variable is provided by rapidity difference $\Delta Y = Y(D) - Y(\overline{D})$. The rapidity or $Y = \frac{1}{2}\ln\left(\left(E + P_{\|}\right) / \left(E - P_{\|}\right)\right)$ approaches the longitudinal velocity in the nonrelativistic limit, but with the added virtue that a rapidity difference is relativistically invariant. Finally, the invariant mass of the $D\overline{D}$ pair measures transverse as well as longitudinal kinematic correlations.

Figure 12 compares the $D\overline{D}$ kinematic correlations observed in E687 data to the predictions of the JETSET-PYTHIA Monte Carlo[6] run with default parameters. There is good agreement between the ΔY and $M(D\overline{D})$ longitudinal correlation variables observed in the data to those predicted by the default JETSET-PYTHIA Monte Carlo. This longitudinal correlation data along with the P_t distribution for inclusive photoproduced D^+'s shown in Fig. 7, and the asymmetry data presented in Sec. 2.4, underscores this LO Monte Carlo's ability to successfully model the important soft physics effects of fragmentation. However, the PYTHIA Monte Carlo gives far too much peaking of $\Delta\phi$ distribution near π and the $P_t^2(D\overline{D})$ distribution near zero. Because the $\Delta\phi$ and $P_t^2(D\overline{D})$ distributions should be sensitive to hard gluon emission, it would be surprising if PYTHIA got these transverse correlations right since it does not incorporate the hard gluon emission processes¶ at NLO illustrated in Fig. 3.

¶JETSET does include bremsstrahlung-like, soft gluon emission in its parton shower fragmentation model.

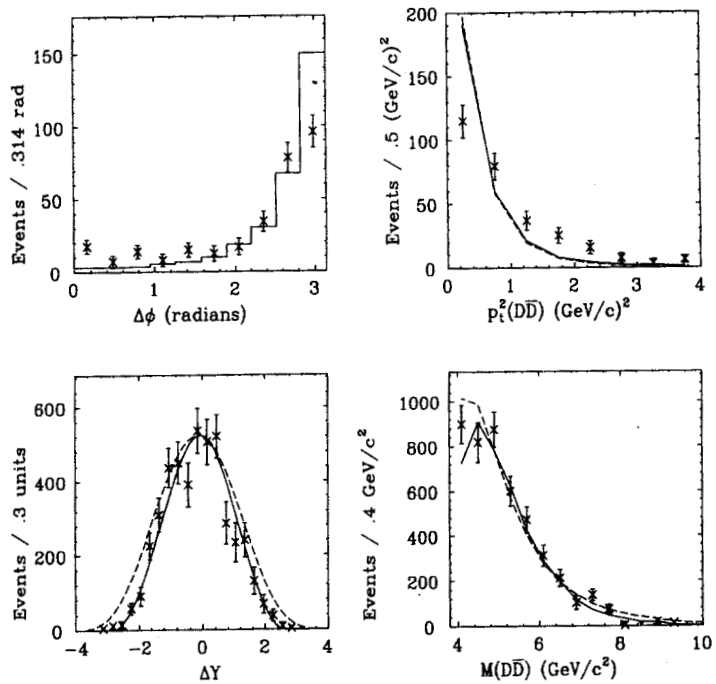

Fig. 12. $D\overline{D}$ kinematic correlations observed in E687 data overplotted with the predictions of the default PYTHIA model. We use the fully reconstructed $D\overline{D}$ sample for the upper row of transverse correlations, and (because of its larger kinematic acceptance domain) the partially reconstructed sample for the lower row which involves longitudinal correlations. The solid curves show acceptance-corrected predictions; the dashed curves show the predictions without acceptance effects.

Indeed, Fig. 13, which compares the NLO predictions of FMNR[3] to the $\Delta\phi$ and $P_t^2(D\overline{D})$ distributions observed by E687, shows that the NLO predictions agree with the data as long as reasonable $< k_t^2 >$ values are used.

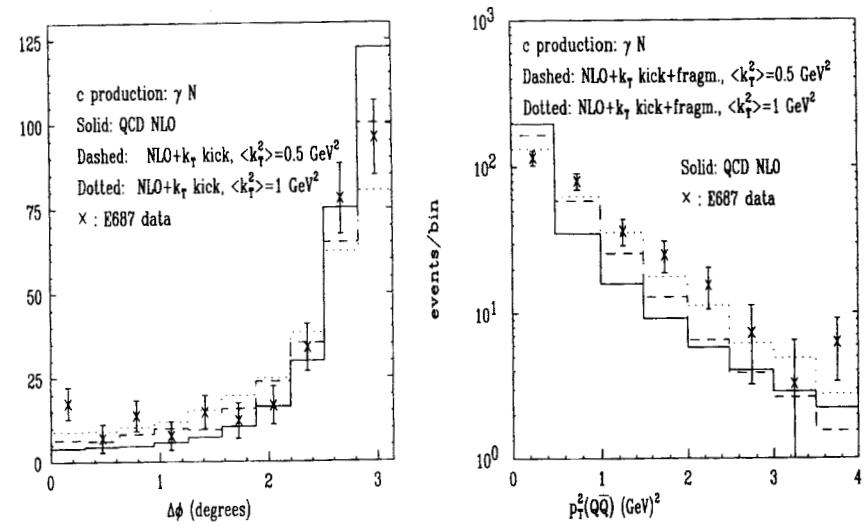

Fig. 13. Overlay of the NLO predictions for the $\Delta\phi$ and $P_t^2(D\overline{D})$ distributions to E687 data for several $< k_t^2 >$ choices.

2.4 Charm-Anticharm Asymmetries

In lowest order QCD, the charm and anticharm quark are produced symmetrically in photoproduction and hadroproduction. In hadroproduction, at next to leading order, QCD introduces small ($\approx 1\%$) asymmetries in quark momenta due

to interference between contributing amplitudes. As we shall see, however, a significant degree of $c\bar{c}$ asymmetries can naturally arise through the fragmentation process. Figure 14 illustrates the mechanism responsible for a photoproduced $c\bar{c}$ asymmetry in the JETSET-PYTHIA model. As shown in Fig. 14, the dominant source of charm-$\overline{\text{charm}}$ asymmetry in the JETSET-PYTHIA model for photoproduction arises through the differences between the momentum fraction of the target nucleon remnant carried by the effective quark and di-quark color poles. The di-quark and quark remnants should be viewed as effective color pole descriptions rather than actual quarks or di-quarks. As such, there is no reason to assume that their momentum fractions are the same as the quark momentum distributions measured in deep inelastic leptoproduction. In the default JETSET-PYTHIA, the effective quark is drawn with a momentum fraction given by $dN/dx \propto (1-x)^3/x$ which has the soft $1/x$ dependence expected for a sea quark distribution. Since at the energies employed by E687 the gluons are typically very soft as well, the default PYTHIA puts nearly all of the nucleon momentum fraction into the effective di-quark. The very different momentum fractions carried by the quarks and di-quarks in the default PYTHIA Monte Carlo leads to asymmetries in the charm-$\overline{\text{charm}}$ particle momentum distributions which are much stronger than those observed in the E687 (Ref. 8) data. On the other hand, an alternative PYTHIA effective quark distribution called the "counting rule" option draws the effective quark momentum fraction according to a much harder spectrum: $dN/dx \propto (1-x)$. When one uses the counting rule option, 1/3 of the nucleon remnant momentum on average is carried by the effective quark and 2/3 is carried by the di-quark. A counting-rule Monte Carlo predicts significantly less charm-$\overline{\text{charm}}$ asymmetry, which is in good agreement with the experimental data.

Figure 15 compares the kinematic variation of the photoproduced D^+/D^- measured asymmetry to the PYTHIA-JETSET Monte Carlo for sea-like (default) and counting rule effective quark momentum fractions. The more symmetrical counting rule model does a very good job at matching the kinematic trends and level of the D^+ asymmetry observed in the E687 data. It is also a reasonable match to the overall level of photoproduced asymmetry observed for other charm decay modes‖ as shown in Table 1.

‖Note that different asymmetries are predicted for two different decay modes of the D^o. This is true since the asymmetries are not corrected for experimental acceptance and the two decay modes have different acceptance versus momentum curves.

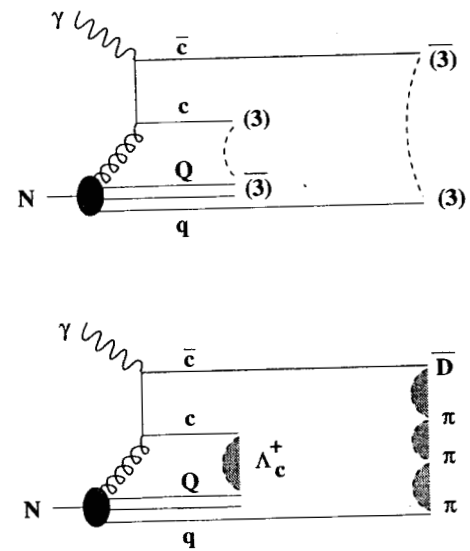

Figure 14: In JETSET, strings are drawn between the triplet and anti-triplet color poles. Final-state hadrons are produced as these strings fragment. Quarks are color triplets; antiquarks are color anti-triplets. In photon-gluon fusion, the initially colorless nucleon emits a color octet gluon. The nucleon remnants must therefore form a color octet to "cancel" the color of the gluon. JETSET achieves color conservation by resolving the nucleon remnants into an anti-triplet, effective di-quark (Q), and a triplet, effective quark (q). Because the c quark must dress with the q remnant and the $\bar{c}$ quark must dress with the Q remnant, a difference between the quark and di-quark momenta fraction distributions will lead to an asymmetry between the momenta spectra of the charmed and anti-charmed hadrons.

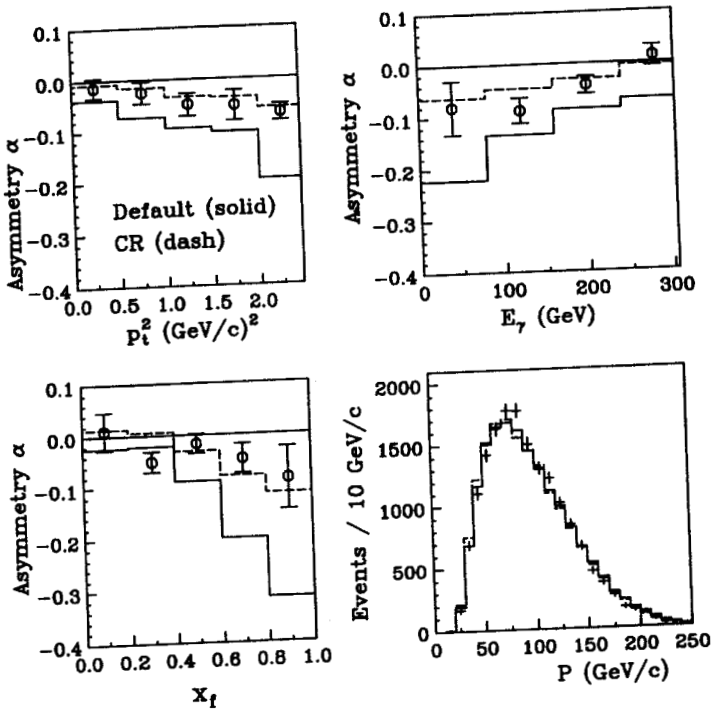

Figure 15: The asymmetry $\alpha = (N(D^+) - N(D^-)) / (N(D^+) + N(D^-))$ in bins of $P_t^2(D^\pm)$, incident photon energy, and $X_F(D^\pm)$ for accepted $D^\pm$ photoproduced from E687. The data is indicated with error bars, the sea-like effective quark predictions are solid and the counting rule effective quark predictions are dashed. The lower right corner compares the total lab momentum spectrum for $D^\pm$ candidates to the two models. In contrast to the asymmetry, the lab momentum spectrum is insensitive to the assumed effective quark momentum distribution.

Table 1. Observed asymmetry α (%) compared to predictions.

Decay Mode	E687 Data	Sea-Like	Counting Rule
$D^+ \to K^-\pi^+\pi^+$	-3.8 ± 0.9	-10.4 ± 0.4	-2.9 ± 0.3
$D^{*+} \to D^0\pi^+ \to (K^-\pi^+)\pi^+$	-6.4 ± 1.5	-9.2 ± 0.7	-2.4 ± 0.5
$D^{*+} \to D^0\pi^+ \to (K^-\pi^+\pi^+\pi^-)\pi^+$	-4.0 ± 1.7	-9.2 ± 0.8	-3.0 ± 0.5
$D^0 \to K^-\pi^+$ (no D^*-tag)	-2.0 ± 1.5	-5.1 ± 0.6	-1.6 ± 0.4
$D^0 \to K^-\pi^+\pi^+\pi^-$ (no D^*-tag)	-1.9 ± 1.5	-9.9 ± 0.5	-2.9 ± 0.4
$D_s^+ \to K^-K^+\pi^+$	2.5 ± 5.2	9.7 ± 1.7	2.5 ± 0.7
$\Lambda_c^+ \to pK^-\pi^+$	3.5 ± 7.6	21.5 ± 0.7	-7.7 ± 0.6

Recently, the E791 Collaboration[49] studied the kinematic asymmetry from their ≈74,000 event sample of D^+ produced with 500 GeV π^-'s incident on a target consisting of four diamonds and one platinum foil. The asymmetry measured by E791 (with the opposite convention as ours) is shown in Fig. 16. The basic trend of an asymmetry which favors more D^-'s at larger X_F is the same trend observed in the photoproduction data of Fig. 15, but the level of asymmetry is much larger in hadroproduction.

This asymmetry pattern has been previously observed by other groups[9] who study charm hadroproduction where it goes under the name of the leading particle effect (since the D^- contains the same $\bar{u}$ quarks found initially in the π^- projectile). As is the case for photoproduction, the asymmetry observed in hadroproduction is a sensitive probe of fragmentation effects since the $c\bar{c}$ asymmetry predicted in NLO for charm quarks is very small. Again, the overall level of asymmetry in the default PYTHIA Monte Carlo exceeds the data but can be matched once one increases the $< k_t^2 >$ to 1 GeV^2 and increases the charmed quark mass from 1.35 to 1.7 GeV. The pattern of asymmetry predicted by the Vogt-Brodsky[50] intrinsic model does not really match the data although a better match might possibly be obtained by varying some parameters.

2.5 Production Dynamics Summary

Although most of my discussion involved the QCD charm photoproduction process, many of the same conclusions apply to high-energy charm hadroproduction.

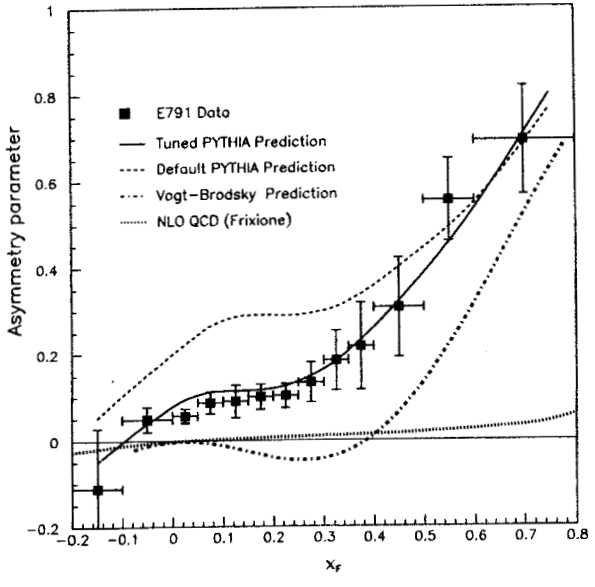

Fig. 16. Comparison of E791's (Ref. 49) measurement (error bars) to various models for the π^- hadroproduction asymmetry. Their asymmetry convention is a "leading particle" asymmetry with the D^- being the "leading particle," which has the opposite convention as that used in Fig. 15 and Table 1 for E687. Overlayed on the figure are the predictions of default PYTHIA, a tuned PYTHIA model, the intrinsic charm model of Vogt and Brodsky,[50] and the FMNR NLO prediction for charmed quarks which shows a very mild asymmetry for the bare charmed quarks.

The NLO photon-gluon fusion calculations of FMNR do a good job at reproducing the photoproduced cross section over a large range of photon energies from 20 GeV to over 30 TeV. Such calculations require a choice of charmed quark mass, renormalization scale, and gluon momentum fraction distribution.

Fragmentation effects play an important role in the P_t and X_F distribution for photoproduced charmed particles. In particular, in the absence of fragmentation effects, NLO calculations predict a significantly harder tail to the P_t^2 distribution for photoproduced charmed mesons than is observed in E687 data. Studies of the kinematic correlations between fully and partially reconstructed $D\overline{D}$ pairs provide incisive tests of QCD-inspired fragmentation models such as the LO JETSET-PYTHIA model. Longitudinal correlations such as the rapidity difference between the D and $\overline{D}$ are well-reproduced by PYTHIA, whereas transverse correlations such as the $D\overline{D}$ acoplanarity angle distributions show considerably more smearing in data compared to the PYTHIA Monte Carlo. This difference can be attributed to the hard gluon emission process which occurs at NLO. Indeed, the FMNR NLO calculations predict an acoplanarity distribution which is in good agreement with the data under reasonable fragmentation and k_t assumptions.

Finally, the asymmetry in the momentum spectrum between photoproduced and hadroproduced charmed and anticharmed particles primarily reflects the fragmentation process. The mechanism used in the JETSET-PYTHIA model for color conservation in photon-gluon fusion where the target nucleon remnants appear as effective quark and di-quark color poles provides a natural mechanism for charm-$\overline{\text{charm}}$ asymmetry. The asymmetry predicted by the JETSET-PYTHIA Monte Carlo does a good job at matching asymmetries seen in E687 data provided that a simple counting rule distribution which attributes (on average) 1/3 of the nucleon remnant momentum to the effective quark and 2/3 of the remnant momentum to the di-quark is used. JETSET-PYTHIA also does a good job of predicting the kinematic asymmetry observed in hadroproduction for particular parameter choices.

3 Heavy Quark Decay

A great many tools of QCD have been brought to bear on the issue of heavy quark decay. In this section, we will primarily review the physics of charm rather than beauty decay, since in charm, the QCD corrections to the weak decay process

are particularly important. On the most inclusive level, the lifetimes of weakly decaying charmed particles serve as measurements of the total decay rate. In the absence of QCD effects, the lifetimes of heavy flavor states would depend on the heavy quark alone, rather than the specific charm or beauty particle being considered. Although the lifetimes of the various beauty states are all comparable, the lifetimes of various weakly decaying charm states differ by roughly an order of magnitude. Recent progress has been made in predicting the deviations from a universal charm lifetime due to QCD corrections, through the use of heavy quark expansions in $1/M_Q$.

We will turn next to a discussion of leptonic and semileptonic decays of charmed mesons. These are the simplest exclusive decays to understand since all of the QCD effects can be expressed as modifications to a weak hadronic current through form factors which can be computable in principle using Lattice Gauge Theory. Since all semileptonic decay processes studied thus far have a single final-state daughter hadron, the complications of final-state interactions which plague nonleptonic decays are absent. We next discuss polarization phenomena in charmed baryon decay, an area of charm decay where HQET makes a very interesting prediction.

We conclude with a discussion of nonleptonic charm decays which are generally studied within a framework called factorization. In this framework, two-body charm decays are described by the interaction of two hadronic currents which are similar to those describing leptonic and semileptonic decays. Unfortunately, when several strongly interacting final-state particles are produced, they can continue to interact after their formation, via final-state interactions. These final-state interactions can significantly distort the factorization predictions for, *e.g.*, branching ratios into specific two pseudoscalar final states by creating an *a priori* unknown phase shift between interfering amplitudes. These same strong phase shifts can be independently studied through interference between the various quasi-two-body decay amplitudes which contribute to a particular three- or four-body charm decay.

3.1 Charm Particle Lifetimes

There are seven known weakly decaying charmed particles with experimentally measurable lifetimes. Last year, the lifetime for the heaviest of these, the Ω_c^o (css) (2704), was measured for the first time. As you can see from the compendium of lifetime results measured by E687 shown in Table 2, there is roughly an order of magnitude difference between these seven lifetimes.[10] Before discussing the physics implications of such measurements, I would like to use a few words to explain how such measurements are made.

Table 2. E687 lifetime measurements (in psec).

D^+	D^o	D_s^+
$1.048 \pm .015 \pm .011$	$0.413 \pm .004 \pm .003$	$0.475 \pm 0.020 \pm 0.007$
Λ_c^+ (udc)	Ξ_c^+ (csu)	Ξ_c^o (csd)
$0.215 \pm 0.016 \pm 0.008$	$0.41^{+0.11}_{-0.08} \pm 0.02$	$0.101^{+0.025}_{-0.017} \pm 0.005$
Ω_c^0 (css)		
$0.089^{+0.027}_{-0.020} \pm 0.028$		

3.1.1 Lifetime Measurement

Most experimental information on charmed particle lifetimes comes from fixed-target experiments employing vertexing techniques. In order to tag charm, one generally requires a minimal detachment between the primary and charm decay vertex of $\ell > \mathcal{N}\ \sigma_\ell$, where σ_ℓ is the event-by-event estimate of the experimental resolution on the detachment and $\mathcal{N}$ is the minimum detachment in units of the computed measurement error, σ_ℓ, deemed adequate to ensure a clean enough charm sample (often a 5–10 σ_ℓ cut is used). It might seem that the use of an event-dependent minimum lifetime cut which is required to isolate charm might complicate the process of measuring a charm particle lifetime. Actually, these complications are actually fairly minor. E687 and most other groups fit their lifetime evolution data using what is known as a reduced proper time variable, $t' \equiv (\ell - \mathcal{N}\ \sigma_\ell)\,/(c\beta\gamma)$, where the $(c\beta\gamma)^{-1}$ converts the distance to a proper time including time dilation, and the $\mathcal{N}\ \sigma_\ell$ piece effectively starts the clock at the point of the minimum detachment cut. An exponential decay distribution is exponential no matter when the clock is started. Given that the error on the detachment (σ_ℓ) is approximately independent of ℓ and that the acceptance usually has only a weak

dependence on ℓ, the reduced proper time for a decaying state will closely follow an exponential distribution expected for a state of lifetime τ: $dN/dt' \approx \exp(-t'/\tau)$.

We generally make binned likelihood fits to the reduced proper time (t') distributions by minimizing a log-likelihood variable w of the form:

$$w = -2\sum_{i}^{\text{bins}} \ln \mathcal{P}(n_i;\mu_i) - 2\ln \mathcal{P}(N_{\text{sidebands}};2B)$$

$$\text{where } \mathcal{P}(n_i;\mu_i) \equiv \frac{{\mu_i}^{n_i}\, e^{-\mu_i}}{n_i!} \text{ and } \mu_i = S\, f(t_i')\, e^{-t_i'/\tau} + B\, b_i. \qquad (3)$$

A few words on Eq. (3) might help. The departure from a pure $\exp(-t_i'/\tau)$ form due to acceptance variation and absorption of the charmed particles or decay products as they travel through the target are included through the factor $f(t_i')$ which is deduced via Monte Carlo simulation.* The fit maximizes the Poisson probability that t' bin populations $\{n_i\}$ of events in the signal region (about, *e.g.*, the D^o) matches the number expected $\{\mu_i\}$ for a given lifetime τ and background level B which are the two fit parameters. The fit accomplishes this by minimizing w with the extra factor of -2 included so that the $\pm 1\sigma$ errors correspond to changes of $w - w_{\min} = 1$. Figure 17 illustrates the background subtraction method used in this type of fit. This procedure should be valid and free of systematics to the extent that time evolution for the background under the signal can be adequately determined by events with masses near the signal peak and that proper time resolution is small compared to the lifetime.

For the case where $\sigma(\tau) \ll \tau$ † and the background level is small, the anticipated fractional statistical error on the lifetime is given by $\sigma_\tau/\tau = 1/\sqrt{N_{\text{sample}}}$. This means that a $\pm 1\%$ statistical error on τ (which is comparable to present systematic errors due to background uncertainties) would require about 10,000 reconstructed events. This yield has already been achieved in experiments such as E687 and E791. Interestingly enough, the lifetime knowledge for the D system is already comparable to that for kaons: $\sigma_\tau/\tau = 0.1\% \rightarrow 0.8\%$ for kaons.

*E687 uses a vertex finder which is efficient even at very small detachments, and hence the correction functions $f(t_i')$ for our experiment are nearly constant. The one exception is that $f(t_i')$ cuts off at long t' for the very long-lived D^+ since it has a nonnegligible probability of decaying downstream of our silicon microstrip vertex detector!

†In a fixed-target experiment, $\sigma_\ell \propto P(\text{charm state})$, and hence, one has a resolution on t' which is independent of momentum and about the same for all fully reconstructed charm states. For E687, $\sigma(t') \approx \tau(D^o)/10$, and hence for many of the measurements reported in Table 2, proper time resolution is unimportant.

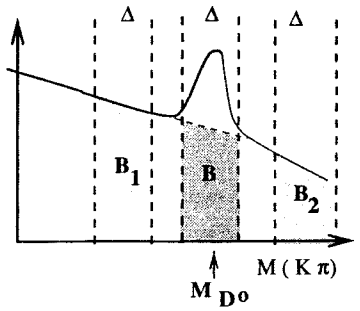

Fig. 17. A sketch of the histogram used to deduce parameters for the lifetime fit described by Equation 3. The log-likelihood variable w is constructed from the population of signal region events found in each bin of reduced proper time (t_i'). The normalized background shape b_i is taken directly from events falling in the equal width, sideband regions marked B_1 and B_2. Information which ties the fit parameter B to the average of the number of events in each sideband is communicated to the fit through the inclusion of the term $-2\ln \mathcal{P}(N_{\text{sidebands}};2B)$.

3.1.2 Lifetime Physics

Lifetimes represent the most inclusive way of looking at charm particle decay. The lifetime is related to the total decay width via the expression:

$$\Gamma_T(C_x) = \sum_i \Gamma_i = \frac{\hbar}{\tau(C_x)}. \qquad (4)$$

The partial width ratio (Γ_i/Γ_T) gives the fraction of times a given charm particle C_x will decay into a particular final state i. Theoretical predictions for the decay rate into a given final state, i, are generally expressed in terms of the partial width Γ_i. In the absence of the quark re-arrangement effects permitted by QCD, charm particles would be expected to proceed by the naive spectator model depicted in Fig. 18. We thus expect in the naive spectator model a universal charm decay width given (in the absence of HO corrections and QCD effects) by:

$$\Gamma_T = (2+3)\,\Gamma_o \text{ where } \Gamma_o = \frac{G_F^2 m_c^5}{192\pi^3}\,|V_{cs}|^2.$$

$$\text{Scaling from the muon : } \tau_C = \frac{1}{5}\left(\frac{0.105}{1.5}\right)^5 2.2\times 10^{-6} = 7\times 10^{-13}\ s. \qquad (5)$$

Of course, given the fact that the charm lifetimes are not universal but differ by an order of magnitude, there must be additional nonspectator diagrams which

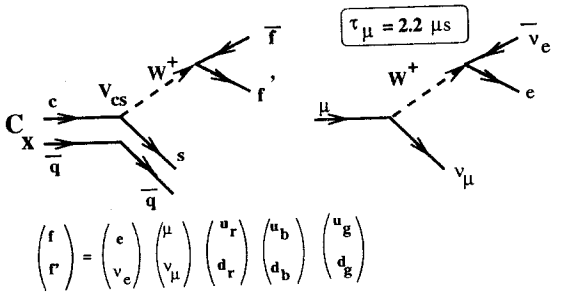

Figure 18: In the naive spectator model, the lifetime of charmed particles should have a universal value which can be estimated by scaling from the known muon lifetime of 2.2 μs. When scaling decay rates, one would need to consider the fact that five low mass final states are available for the charmed quark (two lepton generations and three color multiplets of the first quark generation), and that the charm quark has a much larger decay phase space owing to its much larger mass.

contribute differently for the various charm species. Figure 19 gives examples of nonspectator diagrams which could account for lifetime differences amongst the charmed mesons. Although it is relatively easy to imagine nonspectator decay processes that differentiate among the charmed particles, it has been more difficult to assess their relative importance until recently. Systematic progress has been made by the use of Heavy Quark expansion techniques which include QCD corrections as parameters of an expansion for the semileptonic and nonleptonic widths of the form[11-12]:

$$\Gamma_{SL} = \Gamma_0 \left(1 + \frac{B_2}{m_c^2} + \frac{B_3}{m_c^3} + ...\right)$$

$$\Gamma_{NL} = N_c\, \Gamma_0 \left(1 + \frac{C_2}{m_c^2} + \frac{C_3}{m_c^3} + ...\right)$$

$$\text{where } \Gamma_0 = \frac{G_F^2\, M_Q^5}{192\pi^3}\, |V_{Qq'}|^2. \qquad (6)$$

The expansion of Eq. (6) has some appealing as well as disturbing aspects. As $M_Q \to \infty$, one recovers the predictions of the naive spectator model illustrated in Fig. 5 which features a universal single-generation decay width Γ_0 which depends on the CKM matrix element and the quark mass that controls the size of phase space available to the decay products. Hence, the lifetimes of various beauty particles should be fractionally much closer than those for charm owing to the

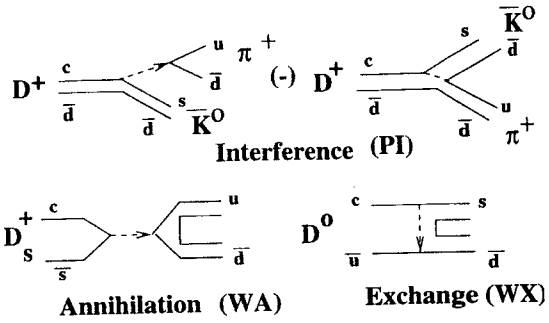

Figure 19: D^+ decays always have two ways of re-arranging the quarks $W^+ \to u\bar{d}$ into the final-state mesons. Because this involves fermion exchange, one expects a destructive (Pauli) interference between the interfering amplitudes which will suppress the rate for D^+ decay and enhance the D^+ lifetime. The $c\bar{s}$ quarks comprising the D_s^+ have a CKM-allowed coupling directly to a virtual W^+ giving a CKM-favored weak annihilation contribution unique among mesons to the D_s^+. Finally, the D^o has a CKM-allowed W^+ exchange contribution which among mesons is unique to the D^o.

heavier b-quark mass. The processes which differentiate among the various heavy quark species such as those depicted in Fig. 19 contribute to the coefficient C_3.

Tables 3 and 4, taken from Bigi,[12] compare various experimental lifetime ratios to the predictions of a $1/M_Q$ expansion which uses various inputs, including theoretical estimates for the leptonic decay constants of the D and the mass and mass splitting pattern among various charm hadrons.

As expected, the lifetimes are much closer between the species measured for the beauty sector than is the case for the charm sector. The rough factor of two difference between the D^+ and D^o lifetime suggests that the PI mechanism, shown in Fig. 19, is important, while the relative equality between the D^o and D_s^+ lifetime suggests that the WA process must not be very important.

To the heavy quark experimentalist, Eq. (6) contains the ominous prediction that the semileptonic widths are not universal among the various charm or beauty species. This is disturbing news since most of our present knowlege of charm particle branching ratios beyond the well-known D^+ and D^o absolute branching

Table 3: Comparison of data to $1/M_Q$ expansion in the charm sector.

Lifetime Ratio	QCD $1/M_c$ exp	Data
D^+/D^o	≈ 2	2.547 ± 0.043
D_s/D^o	≈ 1	1.125 ± 0.045
Λ_c/D^o	≈ 0.5	0.51 ± 0.05
Ξ_c^+/Λ_c	≈ 1.3	1.75 ± 0.36
Ξ_c^+/Ξ_c^o	≈ 2.8	3.57 ± 0.91
Ξ_c^+/Ω_c	≈ 4	3.9 ± 1.7

Table 4: Comparison of data to $1/M_Q$ expansion in the beauty sector.

Lifetime Ratio	QCD $1/M_b$ exp	Data
B^-/B_d	≈ 1	1.04 ± 0.05
B_s/B_d	≈ 1	0.98 ± 0.08
Λ_b/B_d	≈ 0.9	0.76 ± 0.06

fractions depend on the assumption of a universal semileptonic width.‡ The hope that there might be a universal semileptonic width is based on experience with the $D^+ - D^o$ system where it was noted that the ratio of the D^+/D^o semileptonic width was approximately the ratio of the D^+/D^o lifetime[13]:

$$\frac{\mathcal{B}_{SL}(D^+)}{\mathcal{B}_{SL}(D^o)} = 2.3 \pm 0.4 \pm 0.1 \quad \approx \quad \frac{\tau(D^+)}{\tau(D^o)} = 2.54 \pm 0.07. \tag{7}$$

This observation implies that $\Gamma_{SL}(D^+) \approx \Gamma_{SL}(D^o)$ since $\mathcal{B}_{SL} = \Gamma_{SL}/\Gamma_T$ and $\Gamma_T(D^o)/\ \Gamma_T(D^+) = \tau(D^+)/\tau(D^o)$. However, it is really not correct to infer a universal semileptonic width for all charm species based on this evidence since the D^+ and D^o are in the same isodoublet and the $c \to s$ transitions involved in semileptonic decays will transform as $\Delta I = 0$. Nonetheless encouraged by the possibility of a universal Γ_{SL}, groups have been estimating absolute branching fractions through the technique suggested by Eq. (8).

$$\mathcal{B}_x = \frac{\#C \to x}{\#C \to SL}\ \mathcal{B}_{SL}\ ,\ \mathcal{B}_{SL} = \frac{\Gamma_{SL}}{\Gamma_T}\ ,\ \Gamma_T = \frac{\hbar}{\tau_C}. \tag{8}$$

One can first infer the semileptonic branching ratio ($\mathcal{B}_{SL}$) using the measured lifetime of the state (τ_C) and the value of a "universal" Γ_{SL} measured from the average of the known D^+ and D^o values. Next, the absolute branching fraction into state x can be measured relative to the inferred $\mathcal{B}_{SL}$ by measuring the fraction of times the state decays into the x or SL final state. Although the assumption of a universal Γ_{SL} is invalid, the expected variance according to Bigi[12] is not too large. The expected relative ratios of Γ_{SL} are shown in Table 5.

Table 5. Expected relative values for Γ_{SL}.

D^+	D^o	D_s^+	Λ_c^+	Ω_c^o
1	1	≈ 1	≈ 1.5	≈ 1.2

‡Absolute branching fractions for the D^+ and D^o can be obtained in e^+e^- annihilation just above charm threshold by studying events where both charmed particles are reconstructed. Alternatively, one can tag the presence of a D by kinematically tagging pions from $D^* \to \pi D$ using techniques similar to those described in Sec. 2.3 and count the number of times the tagged D decays into a specfic final state.

3.2 Leptonic Decays of the D_s^+

There has recently been a new measurement of $D_s^+ \to \mu^+\nu$ by the E653 Collaboration. Figure 20 illustrates several features of the D_s^+ decay process. Nature

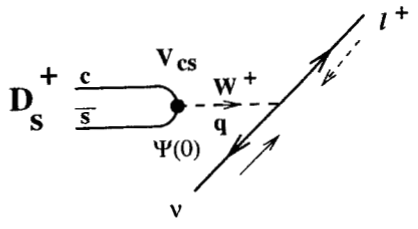

Figure 20: The D_s^+ leptonic decay has the $c\bar{s}$ quarks coupling to the virtual W^+ carrying a four-momentum q_μ with a CKM-favored coupling constant. The virtual W^+ then decays into an ℓ^+ and a left-handed ν. Since the D_s^+ is spinless, the ℓ^+ must emerge left-handed in order to conserve angular momentum along the lepton decay axis. A right-handed antilepton has a highly suppressed $V-A$ coupling. In the context of a quark model, this process provides information on the quark wave function near the origin.

handles the fact that the ℓ^+ is forced into the "wrong" helicity state by suppressing the decay width by two powers of the charged lepton mass as shown in Eq. (10). This means that the only nonnegligible leptonic decays for the D_s^+ will be into taus and muons (with tau's being favored by a factor of ≈ 10.) Because the $\tau^+\nu$ decay includes at least two missing final state neutrinos, it is very hard to experimentally reconstruct, which makes the muonic decay the decay of choice among experimentalists.

Equation (9) shows the structure of the leptonic decay amplitude which is a current × current interaction with one current being the familiar $V-A$ current comprised of the leptons and the other current being an *a priori* unknown current involving the D_s^+,

$$\mathcal{M} = \frac{G_f}{\sqrt{2}}\, \bar{u}_\ell \gamma^\mu\, (1-\gamma_5) v_\nu < 0|\, J_\mu^\dagger\, |D_s^+ > \\ < 0|J_\mu^\dagger|D_s^+ >= i\, V_{cs}\, f_{Ds}\, q_\mu. \qquad (9)$$

This current must be constructed out of the only available vector q_μ which is the four momentum carried by the virtual W^+. The current also contains a potentially

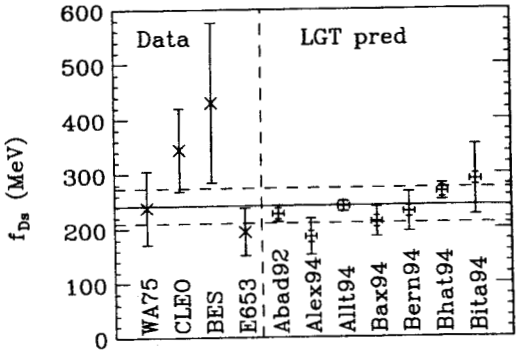

Figure 21: An informal weighted average of the four experimental results gives $f_{D_s} = 242 \pm 32\ MeV$ at $\approx 20\%$ CL level. This value and error form the dashed and solid horizontal lines. Also shown are the Lattice Gauge Theory predictions.

q^2 dependent form factor, but since $q^2 = M^2(D_s^+)$, this form factor just becomes the constant known as the D_s^+ leptonic decay constant. Equation (10) relates the leptonic decay constant to the D_s^+ leptonic width:

$$\Gamma(D_s \to \ell\nu) = \frac{G_f^2 |V_{cs}|^2}{8\pi} f_{D_s}^2\, M_{D_s}\, M_\ell^2 \left(1 - \frac{M_\ell^2}{M_{D_s}^2}\right). \qquad (10)$$

Experimentally, one can measure $f_{D_s}^2$ through the decay width expression by measuring the yield of $D_s^+ \to \mu\nu$ decays to a reference state with a surmised decay width such as $\phi\ell^+\nu$ as discussed in Sec. 3.1.2. Data from BES infers the width directly from the lifetime using a double-tag technique.

Being the theoretically simplest charm decay, there are many theoretical estimates of leptonic decay constants which use a variety of techniques including Lattice Gauge Theory, QCD sum rules, and explicit quark models. The review by Richman and Burchat[14] contains a summary of these calculations and a fuller discussion of the experimental techniques. Figure 21 compares the experimental data[15–18] to the Lattice Gauge calculations. Agreement of the theory with experiment is quite good.

3.3 Semileptonic Decays

The basic heavy quark semileptonic process, depicted in Fig. 22, suggests that a major reason to study semileptonic decays is the measurement of $|V_{Qq}|^2$. Historically,

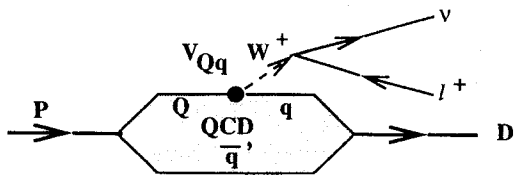

Fig. 22. The basic three-body, semileptonic process where a parent P transforms into a daughter hadron D while emitting a virtual W which materializes into a $\nu\ell^+$ pair. The QCD processes which govern the form factors are complicated but can be computed in principle using Lattice Gauge Theory.

it is true that many CKM matrix elements were first measured through semileptonic decay including nuclear β decay (V_{ud}), $K \to \pi e\nu$ (V_{us}), and more recently, inclusive beauty semileptonic decay at CLEO (V_{ub} and V_{cb}). The grey area of Fig. 22, meant to describe the QCD process by which the $\overline{q}'q$ appears as a fully dressed daughter hadron, is understood in principle but difficult to calculate in practice without approximation.

Only three-body semileptonic decay processes have been studied thus far. All the QCD effects for, *e.g.*, pseudoscalar $\ell^+\nu$ decays are contained in two q^2 dependent form factors which describe how the hadronic weak current between the parent and daughter is constructed from their four momenta:

$$< D|J_\mu^\dagger|P > \;=\; f_+(q^2)\;(P+D)_\mu + f_-(q^2)\;(P-D)_\mu. \qquad (11)$$

Most information is known about the $f_+(q^2)$ form factor since in width expressions, terms involving $f_-(q^2)$ always multiply the charged lepton mass (and hence, they are generally small except for the τ).

For charm semileptonic decays which represent heavy-to-light transitions, the primary theoretical tools have been Lattice Gauge Theory (LGT) and quark models.[§] In LGT,[19] form factors are evaluated as the expectation value of three-point correlation functions describing the parent, current, and daughter. These expectation values involve evaluating integrals by summation over a four-dimensional

[§]In b to c decays, HQET provides considerable understanding of beauty semileptonic decay physics.

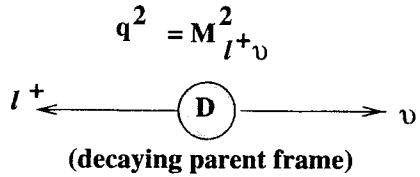

Fig. 23. LGT and Quark Model semileptonic form factor calculations work best when the hadron daughter is at rest. In this configuration, q^2, which is the $\ell^+\nu$ invariant mass, is at q^2_{max}.

space-time lattice of size L and spacing a. Naive computation times would scale as $(L/a)^4$, so there is a computational premium in keeping L as small as possible (but no smaller than the extent of the hadron wave function $\approx 1\ fm$), and a as large as possible (but smaller than the daughter wavelength). Generally, calculations are performed with the daughter at rest in the parent rest frame as depicted in Fig. 23. This is also true of Quark Model calculations which utilize quark wave functions. As the daughter momentum increases and $q^2 \to q^2_{min}$, the form factor probes the tail of the wave function which is the least accurately known part.

Unfortunately, as we will see, the decay intensity of the data is peaked near the maximum daughter momentum or $q^2 \to q^2_{min}$ where theory has the hardest time. For the case of pseudoscalar $\ell^+\nu$ decays, the current of Eq. (11) gives the differential width expression given by Eq. (12),

$$\frac{d\Gamma}{dq^2} = \frac{G_F^2|V_{Qq}|^2|\vec{h}^{(D)}|^3}{24\pi^3}\{|f_+(q^2)|^2 + m_\ell^2\;|f_-(q^2)|^2 ...\}, \qquad (12)$$

where $\vec{h}^{(D)}$ is the three-momentum of the daughter hadron in the D rest frame. These three powers of $|\vec{h}^{(D)}|$ (one from phase space and two from the squared amplitude modulus), severely deplete the intensity near q^2_{max}.

In order to bridge the gap between q^2_{min} where the data are measured and q^2_{max} where the data are predicted, most groups assume the pole form *ansatz* given by Eq. (13),

$$f(q^2) = \frac{f(0)}{1 - q^2/m^2_{\rm pole}}. \qquad (13)$$

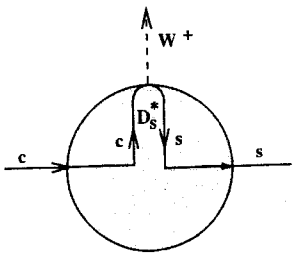

Figure 24: Illustration of the coupling of a virtual W^+ to the $c \to s$ quark. For pseudoscalar $\ell^+\nu$ decays, one can think of the hairpin as a virtual D_s^* vector state comprised of $c\bar{s}$ quarks which contributes a propagator of the form $1/(m^2(D_s^*) - q^2)$.

Expectations are that $m_{\rm pole}$ will be the lowest mass $Q\bar{q}$ resonance with the same spin-parity as the hadronic weak current proportional to V_{Qq}. Figure 24 gives a cartoonish "explanation" of why one might expect a pole-like q^2 dependence with a pole mass given by the spectrum of D^* and D^{**} mesons. Although my version of the pole dominance argument seems *ad hoc*, Burdman and Kambor[20] recently made a detailed dispersion relation calculation to show that contributions of higher poles should be negligible for charm.

Perhaps the most elegant way of thinking about the kinematics of three-body semileptonic processes is via the Dalitz plot which is sketched in Fig. 25. As shown in Eq. (14), the great virtue of the Dalitz plot is that the three-body decay phase space is doubly differential in the Dalitz variables which can be taken as any two of the three possible two-body invariant masses constructed from three final-state daughters. The form ensures that a process with a constant amplitude $\mathcal{M}$ will uniformly populate the Dalitz plot,

$$d^2\Gamma = \frac{|\mathcal{M}|^2}{256\pi^3\, M^3}\, dM_{h\ell}^2\, dM_{\ell\nu}^2 \;=\; \frac{|\mathcal{M}|^2}{256\pi^3\, M^3}\, dM_{hl}^2\, dq^2. \qquad (14)$$

For the case of pseudoscalar $\ell^+\nu$ decays, the $\mathcal{M}$ is not uniform but rather of the form given by Eq. (15),

$$\mathcal{M} \propto f_+(q^2)\; |\vec{h}^{(D)}|\; \sin\theta_{h\ell}^{(q)}. \qquad (15)$$

The $\sin\theta_{h\ell}^{(q)}$ dependence is an easy-to-understand consequence of the $V-A$ helicity rules as illustrated in Fig. 26. This angular factor will cause the decay

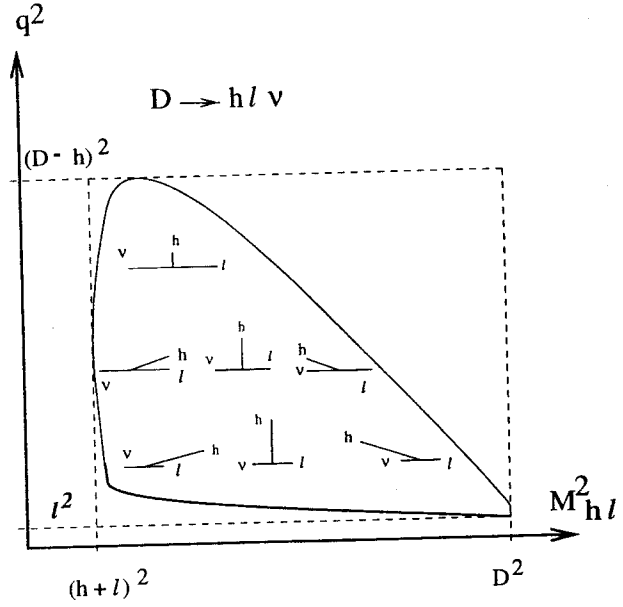

Figure 25: We chose $q^2 \equiv M_{\ell\nu u}^2$ and $M_{h\ell}^2$ as the two conjugate mass variables. The boundaries depend on the masses of the D, final state hadron, and charged lepton, abbreviated as $D, h,$ and ℓ in the figure. Several decay configurations are drawn in the virtual W^+ or q rest frame. The momentum magnitudes of the ℓ, ν, h are fixed at a given fixed q^2 with the lepton momenta increasing and hadron momentum decreasing as q^2 increases. When ℓ^+ and the hadron are collinear, one reaches the left boundary of the plot; when ℓ^+ and the hadron are anticollinear, one reaches the right boundary of the plot. The expression for $M_{h\ell}^2$ is of the form $A - B\, \cos\theta_{h\ell}^{(q)}$.

intensity Dalitz to disappear at the Dalitz boundary where $\theta = 0$. Figure 27 shows simulated Dalitz plots for $D^+ \to K^-\mu^+\nu$, and $\pi^-\mu^+\nu$ decays.

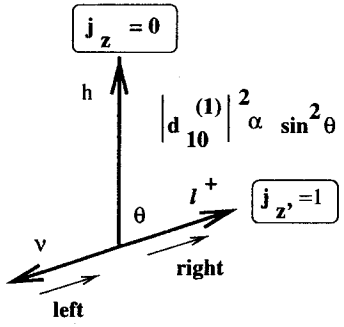

Figure 26: We view the decay in the virtual W^+ rest frame. Since the D is spinless and the hadron, h, is spinless, the virtual W^+ must have zero spin along the axis formed by the hadron. The ν is left-handed while the ℓ^+ is right-handed, which means the virtual W^+ has a spin of zero along the lepton axis. The amplitude for having the W^+ spin with a spin of one along the hadron axis and a spin of one along the lepton axis is proportional to the Wigner D-matrix $d^{(0)}_{10}(\theta) \propto \sin\theta$. The amplitude must clearly disappear when the hadron and lepton axes are either collinear or anticollinear, and the W^+ would need to have two different spin components along the same axes simultaneously.

3.3.1 Experimental Techniques

Semileptonic charm physics presents a real challenge to experimentalists because most experiments which can study charm cannot directly detect the missing neutrino. Although there is often a way of extracting information about the neutrino through missing P_t, the knowledge of the neutrino momentum is often ambiguous and inaccurate. This leaves the experimentalist in a double bind. In contrast to the case of a fully reconstructed final state, there is no well-resolved charm signal peak in the invariant mass distribution, and hence there are many backgrounds where one or more final state particles escapes detection and thus closely resembles the desired final state with a single missing neutrino. One is also faced with

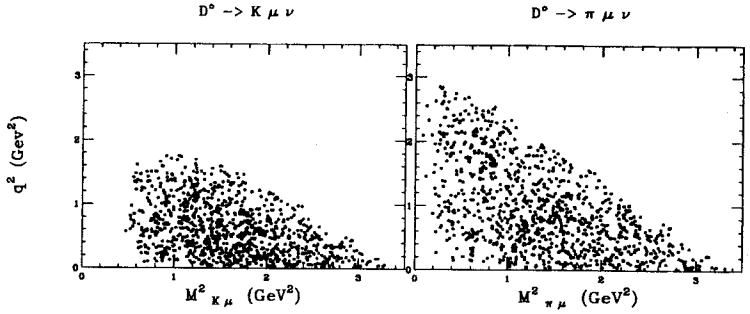

Figure 27: Simulated $D^+ \to K^-\mu^+\nu$ (left) and $D^+ \to \pi^-\mu^+\nu$ (right). The much larger phase space for the pion decay is evident. The point density decreases near the Dalitz boundary and is strongest at low q^2.

the problem of not being able to accurately measure the submasses needed to measure the form factors from the semileptonic final state.

Figure 28 shows how the missing neutrino is reconstructed from the measured D line of flight in a fixed-target experiment like E687. While the neutrino is equally likely to emerge in either hemisphere in the Fig. 28 frame, when the neutrino appears in the backward hemisphere, the charged system tends to be shot forward in the lab frame and gets accepted in the typical fixed-target forward spectrometer. For this reason, most fixed-target results resolve the ambiguity by selecting the solution with the neutrino in the backward hemisphere. Although this properly resolves the ambiguity most of the time, smearing on q^2 due to wrong choices and poor resolution on the D^o line of flight creates a highly significant smearing in q^2.

We turn next to the problem of fitting the semileptonic decay intensity to extract information on form factors. As an example, we describe the technique used by the E687 Collaboration[21] to extract information on $f_+(q^2)$ in Eq. (11) through a fit to the $D^o \to K^-\ell^+\nu$ Dalitz plot. A binned, likelihood fit is made to the $K^-\ell^+_\nu$ Dalitz plot. The idea in such a binned fit is to maximize the agreement between the set of observed bin populations ($\{n_i\}$) and the set of expected populations ($\{\mu_i\}$) for a given set of form factor parameters. This is done by having

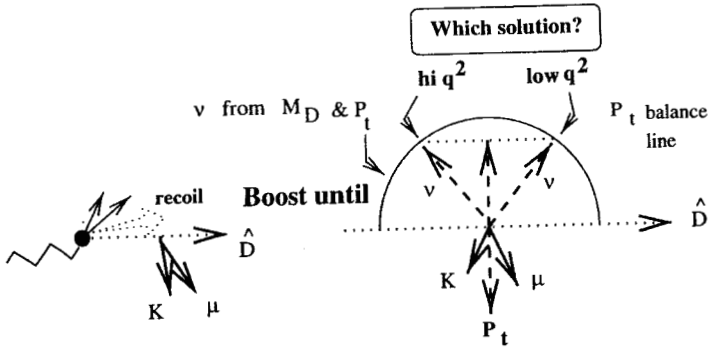

Figure 28: Consider the decay $D^0 \to K^-\mu^+\nu$. By observing tracks from an upstream primary vertex and the downstream vertex, one can reconstruct the D^o line of flight. One boosts the kaon and muon along the D line of flight until the sum of their longitudinal momentum vanishes: *i.e.*, the boosted visible momentum lies transverse to the D^o line of flight. The neutrino momentum must lie on the line which balances the visible P_t. The neutrino momentum must lie on a circle since the magnitude of the neutrino momentum can be calculated from its P_t and the D^o mass. The two circle-line intersections give two ambiguous solutions for the neutrino momentum. In this example, the backward hemisphere solution has the larger q^2 since the angle between the reconstructed neutrino and muon is larger.

the fit vary the form factors to minimize the log-likelihood parameter w given by Eq. (16)

$$w = -2\sum_{i}^{\text{bins}} \ln \mathcal{P}(n_i;\mu_i) \quad , \quad \text{where} \quad \mathcal{P}(n_i;\mu_i) \equiv \frac{{\mu_i}^{n_i}\, e^{-\mu_i}}{n_i!}. \tag{16}$$

The complication in the procedure is that the expected bin populations for a given set of form factors, $\{\mu_i\}$, must reflect the considerable diffusion of events into and out of a given reconstructed q^2 bin due to smearing. In order to properly handle the possible biases and error inflation due to q^2 smearing, most groups use some variant of the fitting technique developed by the E691 Collaboration (Ref. 22), which I will call Los Vegas weighting, and is illustrated in Fig. 29.

3.3.2 $D \to K\ell\nu$

The decays $D \to K\ell\nu$ give the best information on the q^2 dependence of the $f_+(q^2)$ form factor. The most recent, high statistics data comes from E687 (Ref. 21) and CLEO.[23] Figure 30 shows CLEO's $\approx$ 2700 event sample of D^* tagged $D \to K\ell\nu$ events. The (uncorrected) q^2 distribution of the CLEO $K\ell\nu$ sample is shown in Fig. 31.

Figure 32 shows the $D^{*+} - D^o$ mass difference distribution for E687's $\approx$ 430 event sample of $D^{*+} \to (K^-\mu^+\nu)\pi^+$ decays along with their uncorrected q^2 distribution. E687 augmented their D^* tagged sample with an $\approx$ 1900 event inclusive (untagged) event sample of $K^-\mu^+\nu$ decays. Because the $D^* - D$ mass difference cut cannot be applied, there is significantly more background in the untagged $K^-\mu^+\nu$ sample. However, because many of these backgrounds are well-understood, one can reliably subtract their effects by fitting to the $K^-\mu^+\nu$ Dalitz plot using the technique illustrated in Fig. 29. Figure 33 compares observed q^2 and $E_\mu \equiv (M^2_{K^-\mu^+} + q^2 - M^2_K)/(2M_D)$ Dalitz projections to the results computed from the complete fit including backgrounds. Although the background contributions to the Dalitz projections of Fig. 33 are significant, the form factors and relevant branching ratios for each of the major physics backgrounds have already been accurately measured by our own[24,25] and other experiments. Muon misidentification probabilities can be reliably measured using known pions from the decay $K_s \to \pi^+\pi^-$. The parameterized misidentification level was fed into charm Monte Carlo calculations to estimate the shape and level of this background source. The expected population of events in the i'th bin, μ_i, was expressed as a function of the

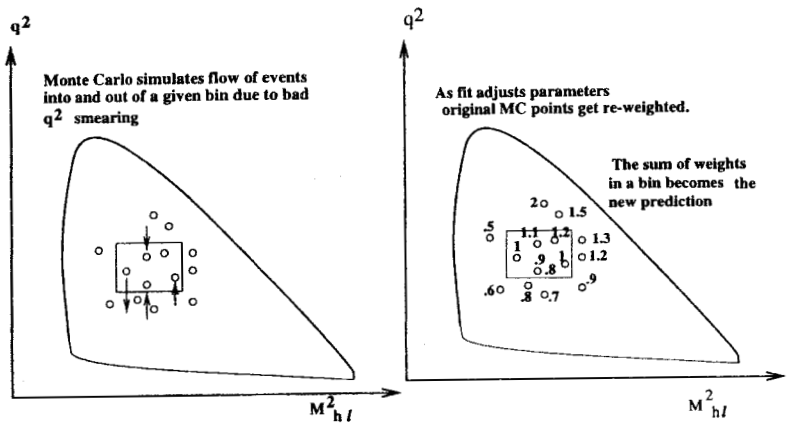

Figure 29: A Monte Carlo simulation using an initial guess for the relevant form factors is used to simulate the q^2 smearing due to neutrino reconstruction. This smearing will cause events to diffuse into and out of each bin. The program saves the generated Dalitz variables as well as the smeared Dalitz variables for each simulated event. As the fitter changes the form factors to minimize w, each simulated event is assigned a weight given by the ratio of the intensity with the new form factors divided by the ratio of the original intensity with the initial guess. The expected number of observed counts μ_i within a bin is computed from the sum of the weights for events falling within the i'th bin. This technique avoids prohibitively computer intensive, separate full Monte Carlo simulations for each iteration of the fit.

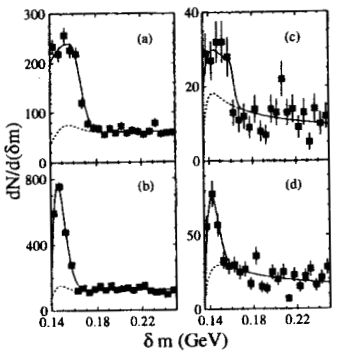

Figure 30: CLEO's $D^* - D$ mass difference for (a) $D^o \to K^- e^+ \nu$, (b) $D^o \to K^- \mu^+ \nu$, (c) $D^+ \to K_s e^+ \nu$, and (d) $D^+ \to K_s \mu^+ \nu$. The background estimates are given by the dashed curves.

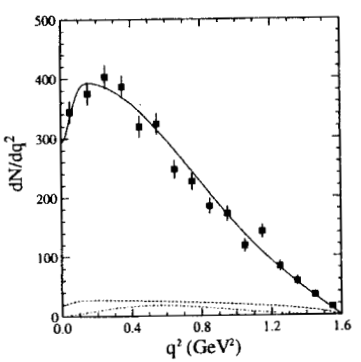

Figure 31: The uncorrected (for acceptance and smearing) q^2 spectrum measured by CLEO in their $\approx$ 2700 event sample of $D \to K\ell\nu$ decays. As suggested by Eq. (12), very few decays are observed near $q^2_{max} \approx 1.9\ GeV^2$.

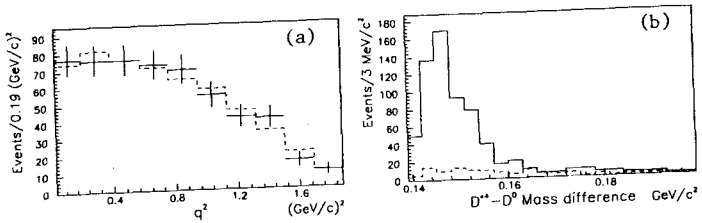

Fig. 32. The $\approx$ 430 event sample of D^* tagged $D^o \to K^-\mu^+\nu$ decays: (a) q^2 distribution, (b) $D^{*+} - D^o$ mass peaks and backgrounds.

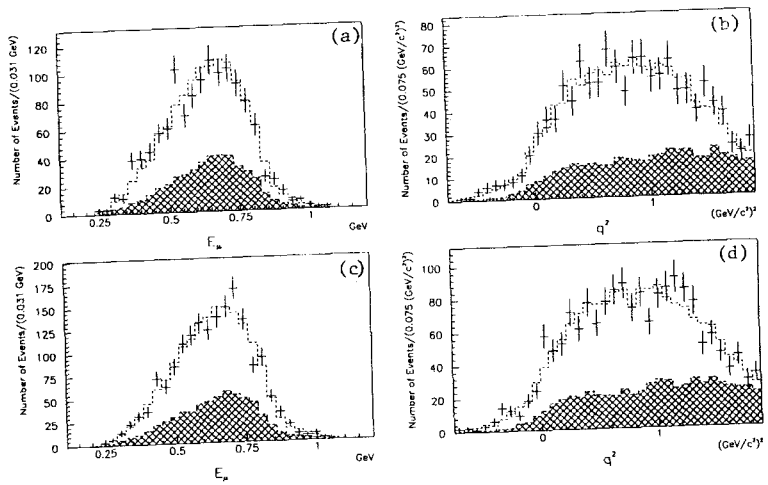

Fig. 33. Projections of the E687 $K^-\mu^+\nu$ Dalitz plot with fits overlayed on the data. Figures (a) and (b) compare projections obtained in 1990 data. Figures (c) and (d) compare projections obtained in 1991 data. A significant hole in our muon wall was inflicted upon us in 1991 to accommodate an experiment located downstream of our apparatus. The shaded region indicates background contributions from $D^+ \to (K^-\pi^+)\mu^+\nu$, $D^0 \to (K^-\pi^o)\mu^+\nu$, $D_s^+ \to \phi\mu^+\nu$, and nonleptonic charm decays where final-state hadrons were misidentified as muons.

yield of actual $D^o \to K^-\mu^+\nu$ events, the various background contributions, $\{b_k\}$, and the pole mass $m_{\rm pole}$ which parameterizes the q^2 dependence of the form factor $f_+(q^2)$.¶ Although the known background contributions, $\{b_k\}$, were allowed to vary throughout the fit, *a priori* information on the anticipated background ($b_k^{(\rm meas)}$) was fed into the fit through the inclusion of a χ^2 contribution to the log likelihood of the form:

$$w = -2 \sum_i^{(bins)} \ln \mathcal{P}(n_i;\mu_i) + \sum_k^{(back)} \frac{(b_k - b_k^{(\rm meas)})^2}{\sigma_k^2}. \qquad (17)$$

The σ_k in Eq. (17) are the initial uncertainties in the background parameters $\{b_k\}$. We used this rather conservative technique so that final statistical errors on the form factors properly reflect uncertainties in the background estimation.

Once the yield of $D^o \to K^-\mu^+\nu$ signal events and pole mass are measured using the fit, the f_+ form factor can be measured via Eq. (18):

$$\Gamma_{K\ell\nu} = \underline{|V_{cs}|^2} \times |f_+(0)|^2 \times \int dq^2 \; H\left(q^2, m^2_{\rm pole}\right)$$
$$\Gamma_{K\ell\nu} = \frac{\hbar\, \mathcal{B}_{K\ell\nu}}{\underline{\tau_{D^o}}} \quad , \quad \mathcal{B}_{K\ell\nu} = \frac{Y_{K\ell\nu}/\epsilon_{K\ell\nu}}{Y_{K\pi}/\epsilon_{K\pi}} \, \underline{\mathcal{B}_{K\pi}}. \qquad (18)$$

The underlined quantities in Eq. (18) are previously well-measured known inputs. The function $H(q^2)$ is the $d\Gamma/dq^2$ expression of Eq. (12) with the $f_+(0)$ and $|V_{cs}|^2$ factored out. By measuring the efficiency-corrected yield of $D^o \to K^-\mu^+\nu$ signal events relative to a reference state ($K^-\pi^+$) with a known branching fraction, $\mathcal{B}_{K\pi}$, observed in the same experiment with similar kinematic cuts, one can measure the branching fraction $\mathcal{B}_{K\ell\nu}$. This $\mathcal{B}_{K\ell\nu}$ can be combined with the D^o lifetime to form a decay width $\Gamma_{K\ell\nu}$. Finally, the integral expression for the decay width can be used to extract $f_+(0)$.

Table 6 gives a summary of the form factor and pole mass obtained in various experiments. Figure 34 shows excellent agreement between the experimental results. Figure 35 compares experimental results on $M_{\rm pole}$. Note that the more recent, high statistics data favors a pole mass which is lower (by $\approx 2\sigma$) than the spectroscopic pole mass.

It is important to point out that the pole mass determinations measure this parameter under the assumption of a pole form. As Fig. 36 shows, over the

¶In this measurement, the $f^-(q^2)/f_+(q^2)$ form factor ratio [see Eq. (11)] was set to the "mid-range" of theoretical expectations $f_-/f_+ \approx -1$. A small systematic error contribution due to uncertainty in this ratio was included.

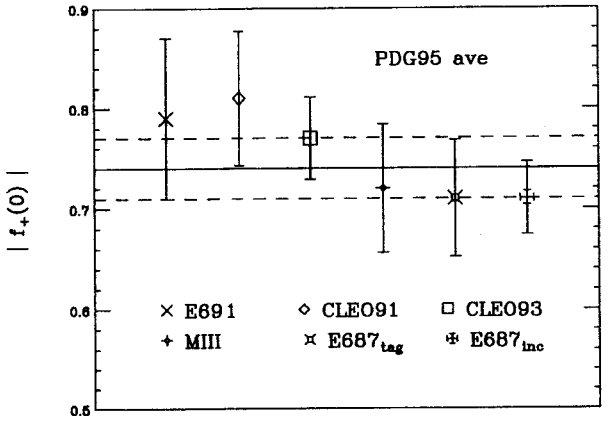

Figure 34: Comparison of the experimental results on $|f_+(0)|$. The weighted average and error are shown by the dashed and solid horizontal lines.

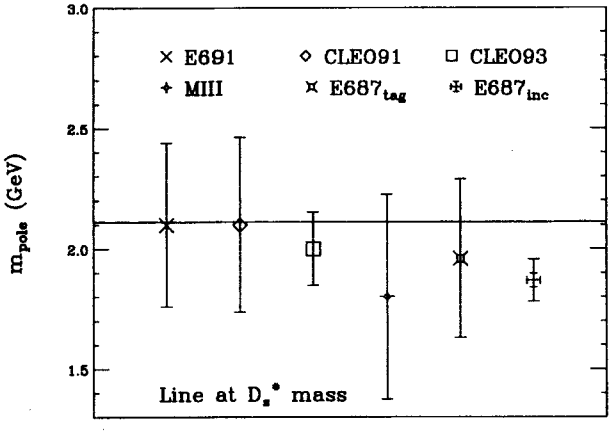

Figure 35: Comparison of the experimental results on $m_{\rm pole}$. The horizontal line is at the D_s^{*+} mass which is the expected pole mass value.

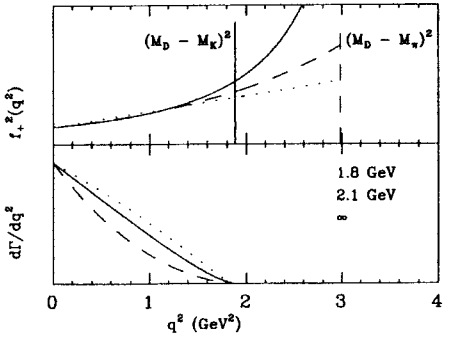

Fig. 36. Upper frame: $|f_+(q^2)|^2$ as a function of q^2 for various q^2 parameterizations which have been drawn to have the same slope and intercept at $q^2 \approx 0$. The kinematic limit for $D \to \overline{K}\ell^+\nu$ and $\pi\ell\nu$ are drawn with vertical dashed lines. The solid curve is the pole form; dashed is exponential; dotted is linear. Lower frame: $d\Gamma/dq^2$ as a function of q^2 for $D \to \overline{K}\ell^+\nu$ decay with three different pole masses. The dashed curve is for $m_{\rm pole} \to \infty$; the solid is for $m_{\rm pole} = 2.1\ GeV$ (the expected value); the dotted is for $m_{\rm pole} = 1.8\ GeV$. The influence of the pole mass on the overall q^2 dependence on $d\Gamma/dq^2$ is rather subtle over the kinematic range probed by $D \to \overline{K}\ell^+\nu$.

Table 6. $K\ell\nu$ form factor results.

Exp.	Mode	m_{pole}	$\mid f_+(0) \mid$
E691	$K^-e^+\nu_e$	$2.1^{+0.4}_{-0.2} \pm 0.2$	$0.79 \pm 0.05 \pm 0.06$
CLEO(91)	$K^-e^+\nu_e$	$2.1^{+0.4+0.3}_{-0.2-0.2}$	$0.81 \pm 0.03 \pm 0.06$
CLEO(93)	$K^-l^+\nu_l$	$2.00 \pm 0.12 \pm 0.18$	$0.77 \pm 0.01 \pm 0.04$
MKIII	$K^-e^+\nu_e$	$1.8^{+0.5+0.3}_{-0.2-0.2}$	$\mid V_{cs} \mid (0.72 \pm 0.05 \pm 0.04)$
E687	$K^-\mu^+\nu_\mu$ tag	$1.97^{+0.43+0.07}_{-0.22-0.06}$	$0.71 \pm 0.05 \pm .03$
E687	$K^-\mu^+\nu_\mu$ incl.	$1.87^{+0.11+0.07}_{-0.08-0.06}$	$0.71 \pm 0.03 \pm 0.02$

kinematic range accessible in $D \to \overline{K}\ell\nu$, a pole form q^2 dependence is nearly indistinguishable from an exponential or linear dependence. This is not true, however, for the decay $D \to \pi\ell\nu$ since the maximum q^2 range in this decay lies much closer to the spectroscopic pole. As Fig. 36 illustrates, over the limited q^2 range probed by the $\overline{K}\ell^+\nu$, the pole mass is essentially a measurement of the normalized slope $f_+^{-1}(0)\ df_+(q^2)/dq^2$. A real check of the pole parameterization in charm semileptonic decay must await a future, well-measured, high-statistics sample of $\pi\ell\nu$ decays.

Figure 37 compares the experimental average to several Quark Model and Lattice Gauge Theory predictions.[26] Agreement between theory and data are quite good. The recent calculations of the LANL (Los Alamos) group[26] which included a study of the q^2 dependence of the $f_+(q^2)$ form factor concluded that $m_{\rm pole} < M\,(D_s^{*+})$, in agreement with the recent trends of the data as shown in Fig. 35.

E687 (Ref. 24) has also presented the first experimental information on the f_- form factor which forms part of the hadronic weak current which is underlined in Eq. (19),

$$< D|J_\mu|K > \ = \ f_+(q^2)\ (D+K)_\mu + \underline{f_-(q^2)}\ (D-K)_\mu. \qquad (19)$$

As shown in Eq. (20), which gives a schematic rendering of partial width expression, the squared lepton mass multiplies the pure $|f_-(q^2)|^2$ as well as interference $2\ f_-(q^2)\ f_+(q^2)$ contributions. For the decay $D^o \to K^-\mu^+\nu$, the effects of $f_-(q^2)$ are to give very small gradients in the Dalitz plot intensity.

$$\frac{d^2\Gamma}{dq^2 dM^2_{K\ell}} = |f_+(q^2)|^2\ \mathcal{A} + \ \underline{M^2_\ell}\ \left(2\ f_-(q^2)\ f_+(q^2)\ \mathcal{B} + |f_-(q^2)|^2\ \ \mathcal{C}\right)$$
$$\mathcal{B} \propto M^2_{K\ell\ \rm max} - M^2_{K\ell} \ - \ \left(q^2 - q^2_{\rm min}\right)/2, \quad \mathcal{C} \propto q^2 - q^2_{\rm min}. \qquad (20)$$

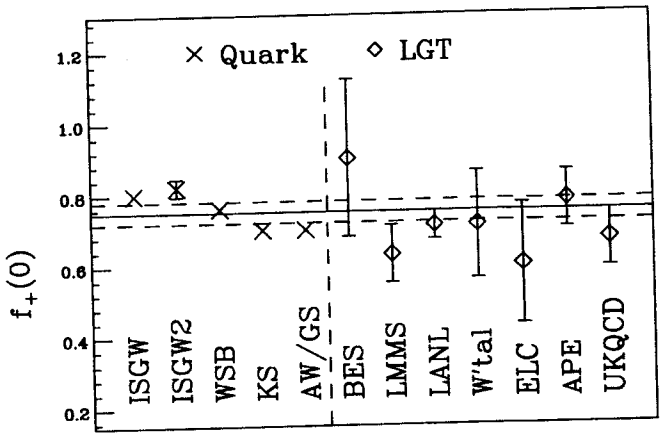

Fig. 37. Comparison of theoretical $f_+(0)$ predictions for $D \to \overline{K}\ell^+\nu$ to the world's data. The first points are quark-model estimates; the last are Lattice Gauge Theory calculations.

Of course, a small error in the $m_{\rm pole}$ parameter will induce a false competing gradient in the Dalitz plot along the q^2 axis by slightly changing the q^2 dependence of the $f_+(q^2)$ form factor. Figure 38 shows likelihood contours on f_-/f_+ versus $m_{\rm pole}$ based on the $\approx$ 430 event E687 sample of D^* tagged $D^o \to K^-\mu^+\nu$ events. From this contour, we conclude $f_-/f_+ = -1.3 \pm 3.5 \pm 0.6$, which is in good agreement with theoretical estimates.[21]

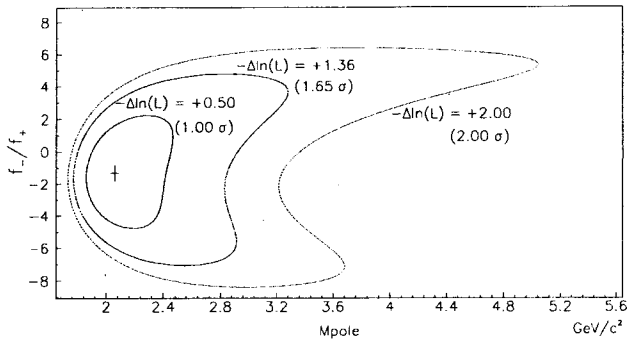

Fig. 38. Contours of constant likelihood for f_-/f_+ versus $m_{\rm pole}$ assuming that f_- and f_+ follow pole forms with the same pole mass. Note that the contour shape shows that a large f_-/f_+ ratio can be compensated by an increased value for $m_{\rm pole}$ which can be understood from Eq. (20) for the case where $|f_-(q^2)|^2 > 2\, f_-(q^2)\, f_+(q^2)$.

3.3.3 $D \to \pi\ell\nu$

As Fig. 39 shows, measurement of $D \to \pi\ell\nu$ / $D \to K\ell\nu$ would seem to provide useful information on the CKM ratio $|V_{cd}|^2/|V_{cs}|^2$. However, as illustrated in Fig. 40, (three-generation) unitarity of the CKM matrix along with experimental information on charm production by high-energy neutrinos on fixed targets and b decays from CLEO already provides V_{cd} measurements which are probably more accurate than the present ability to predict the $\pi\ell\nu/\overline{K}\ell\nu$ form factor ratio. For this reason, the principle motivation for studies of $D \to \pi\ell^+\nu$ decays is to test the ability of the QCD calculational tools to accurately predict the ratio of CKM

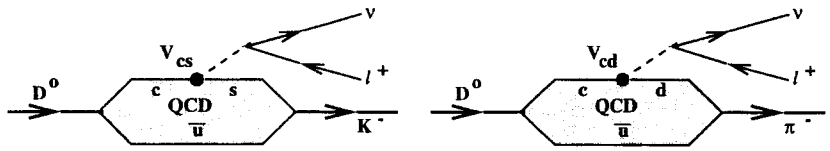

Fig. 39. Apart from possible QCD corrections, the difference between $D \to \pi\ell\nu$ and $D \to K\ell\nu$ are in the CKM matrix element couplings.

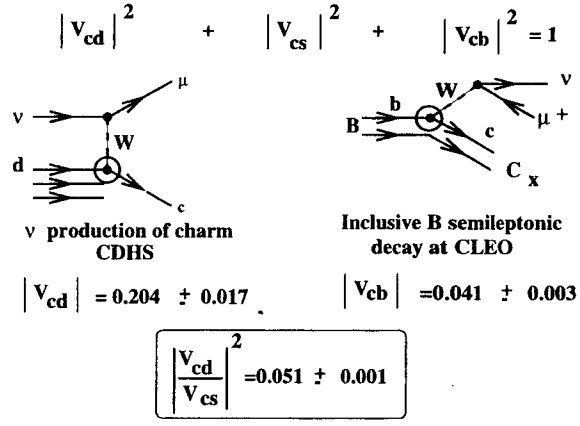

Fig. 40. V_{cd} can accurately be measured by studying the charmed particles produced from incident neutrinos interacting with d valence quarks. Neutrino experiments generally detect the semimuonic decays of charmed mesons. V_{cb} can be determined through measurements of lepton spectrum produced by B decay near threshold at CLEO.

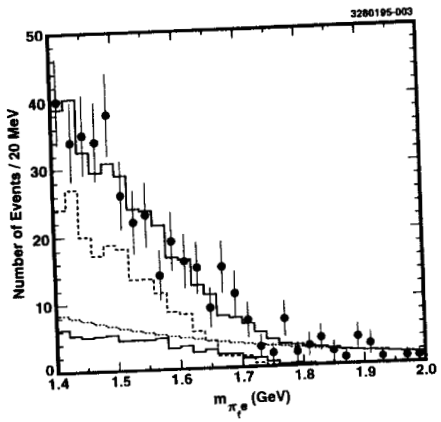

Fig. 41. CLEO $M_{e\pi}$ for events satisfying $M(D^*) - M(D) < 0.160$. The total fit to the $M_{e\pi}$ distribution is shown as a solid histogram. The contribution from backgrounds is shown as the dashed histogram.

favored over CKM suppressed form factors. One hopes that such calculations can ultimately be used to provide CKM information in the b sector.

Recent tagged $D^* \to (\pi^- \ell^+ \nu)\pi^+$ signals are shown in Figs. 41 (CLEO) and 42 (E687). Because the decay $D^o \to \pi^-\ell^+\nu$ is CKM suppressed and therefore somewhat rare, background contamination is a major concern. In E687 (Ref. 28), a major source of background is $D^o \to K^-\ell^+\nu$ where the kaon is misidentified by our Cherenkov system as a pion. Another important class of backgrounds involve semileptonic decays with missing (underlined) daughters such as $D^o \to K^{*-}\ell\nu$, $K^{*-} \to \underline{K^o}\pi^-$ or $D^o \to \rho^-\ell\nu$, $\rho^- \to \pi^-\underline{\pi^o}$. It is possible to significantly suppress missing daughter contributions by requiring a minimum hadron lepton-lepton mass value as illustrated by Fig. 43. The background $D^o \to K^-\ell^+\nu$, $K^- \hookrightarrow \pi^-$, on the other hand, has a $\pi^-\ell^+$ invariant mass distribution which is nearly indistinguishable from that for $\pi^-\ell^+\nu$ and will form a very similar peak in the $M(D^{*+}) - M(D^o)$ mass difference distribution. This means that there is no reasonable way of kinematically distinguishing between the signal and the $D^o \to K^-\ell^+\nu$, $K^- \hookrightarrow \pi^-$ background. For this reason, we jointly fit the $M(D^{*+}) - M(D^o)$ mass difference histograms for both $K^-\ell^+\nu$ and $\pi^-\ell^+\nu$ by summing the binned log likelihoods from both distributions. The contribution of misidentified $D^o \to K^-\ell^+\nu$ events into the $\pi^-\ell^+\nu$

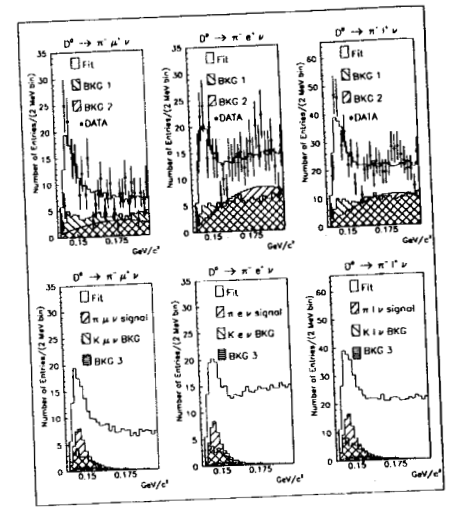

Fig. 42. E687 $M(D^*) - M(D)$ peaks for events satisfying the cut $M_{\ell\pi^-} > 1.1\ GeV$. The first column is $\pi^-\mu^+\nu$ candidates, the second is for $\pi^-e^+\nu$ candidates, and the third is the combined sample. In the legend: BKG1 is the background contribution for misidentified leptons, BKG2 is the background due to actual semileptonic D^o combined with random soft pions to form a false D^{*+}, and BKG3 are misidentified kaons from $D^o \to K^-\ell^+\nu$.

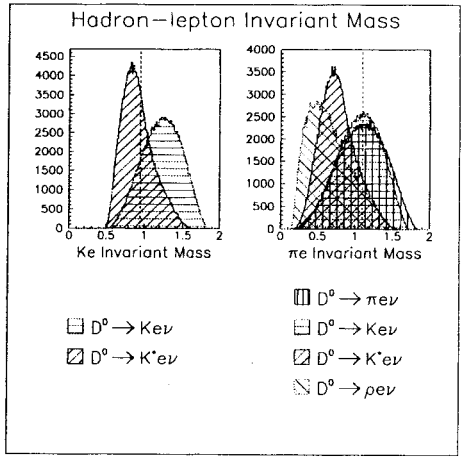

Fig. 43. Simulated hadron-lepton invariant mass distributions for the $D^o \to K^-\ell^+\nu$ signal (left) $D^o \to \pi^-\ell^+\nu$ signal (right) and several background contributions. Missing daughter type backgrounds typically peak below $M^2_{h\ell} < 1\ GeV^2$ and can be significantly reduced through the cut $M^2_{h\ell} > 1.1\ GeV^2$.

$M(D^{*+}) - M(D^o)$ mass difference histogram is proportional to the $D^o \to K^-\ell^+\nu$ signal yield and $K^- \hookrightarrow \pi^-$ misidentification probability, which was parameterized by studies of $D^{*+} \to D^o\pi^+ \to (K^-\pi^+)\pi^+$ which are misidentified in the data as $D^{*+} \to D^o\pi^+ \to (\pi^-\pi^+)\pi^+$ events.

Figure 44 illustrates an interesting systematic on the measurement of the $\pi^-\ell^+\nu/K^-\ell^+\nu$ branching ratio and form-factor ratio. Because the maximum $\sqrt{q^2}$ available in $D^o \to \pi^+\ell^-\nu$ lies only $\approx 300\ MeV$ below the expected D^{*+} pole mass, uncertainties in the effective pole mass‖ will cause significant variations in $|f_+(q^2)|^2$ which will cause intensity variations in the upper reaches of the $D^o \to \pi^-\ell^+\nu$ Dalitz plot. The $M_{\pi^-\ell^+}$ cut used to suppress daughters cuts off the q^2 range and thereby acts like a double-edged sword in measurements of $\pi^-\ell^+\nu/K^-\ell^+\nu$. The $M_{\pi^-\ell^+}$ cut exacerbates measurements of the relative branching fraction since one must extrapolate the number of $\pi^-\ell^+\nu$ below the $M_{\pi^-\ell^+}$ cut in order to measure the efficiency-corrected yield ratio of $\pi^-\ell^+\nu/K^-\ell^+\nu$ events

‖Perhaps several excited D_s^{**} states potentially contribute, or potentially there are contributions from complex cuts.

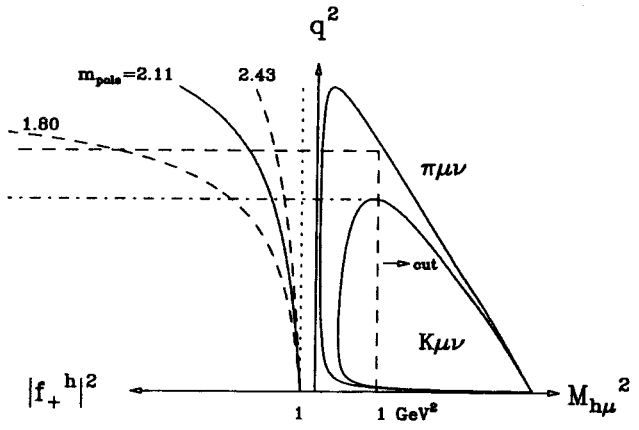

Fig. 44. We show Dalitz plots (right) and form factor variation (left) for several reasonable $m_{\rm pole}$'s. Because of its larger q^2 reach, the $\pi\ell\nu$ Dalitz plot extends into a q^2 range where the $m_{\rm pole}$ uncertainty becomes significant. The $M^2_{\pi^-\ell^+} > 1.1\ GeV^2$ cut eliminates the q^2 region beyond $2.3\ GeV^2$.

over the full Dalitz plot. The variation on the (full Dalitz plot) acceptance including the $M_{\pi^-\ell^+}$ cut as a function of $m_{\rm pole}$ is shown in Fig. 45.

By way of contrast, the $M_{\pi^-\ell^+}$ cut improves the pole mass systematic for the form factor ratio. This ratio follows from the corrected yields of $\pi\ell\nu$ and $K\ell\nu$ events which satisfy the $M_{\pi^-\ell^+}$ cut according to Eq. (21)

$$\frac{Y_{\pi\ell\nu}}{Y_{K\ell\nu}} = \frac{|V_{cd}\ f_+^\pi(0)|^2}{|V_{cs}\ f_+^K(0)|^2}\ \frac{\int dq^2\ |f_+^\pi(q^2)/f_+^\pi(0)|^2\ \mathcal{H}^\pi(q^2)}{\int dq^2\ |f_+^K(q^2)/f_+^K(0)|^2\ \mathcal{H}^K(q^2)},$$

where
$$\mathcal{H}^{(h)}(q^2) = \int_{M^2_{h\ell}\ \rm cut}^{M_D^2} dM^2_{h\ell}\ \ \epsilon(q^2, M^2_{h\ell})\ \left(\frac{d^2\Gamma}{dq^2 dM^2_{h\ell}}\right)_{f_+^{(h)}(q^2)=1}. \qquad (21)$$

The integrals of Eq. (21) are only over the q^2 range satisfying the $M^2_{h\ell}$ cut which limits them to regions farther from the expected $m_{\rm pole}$. The kernels under the integral of Eq. (21) are plotted in Fig. 46. Figure 47 shows the dependence of the final measured form factor × CKM ratio on $m_{\rm pole}$ or alternatively on a linear q^2 parameterization.

Experimental results[27–29] on the $\pi^-\ell^+\nu/K^-\ell^+\nu$ form factor and branching ratio are compared to predictions[30] in Figs. 48 and 49. Agreement between the measured form factor ratios and their predictions is satisfactory.

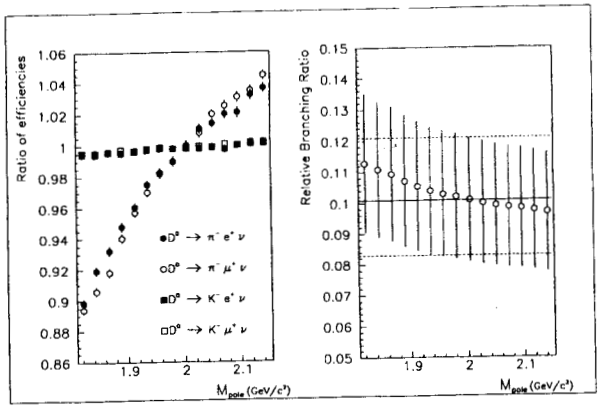

Fig. 45. The $\epsilon(M^2_{h\ell} > 1)$ cut varies by 15% for $\pi\ell\nu$. ϵ for $\overline{K}\ell\nu$ varies much less since its q^2 reach is much smaller.

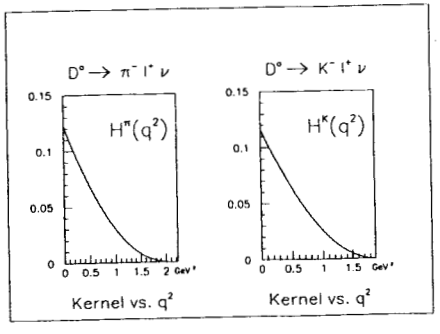

Fig. 46. $\mathcal{H}^\pi$ (left) and $\mathcal{H}^\mathcal{K}$ (right). Our CKM-ff ratio is essentially the ratio of the weighted $<>_\mathcal{H}$'s over these functions.

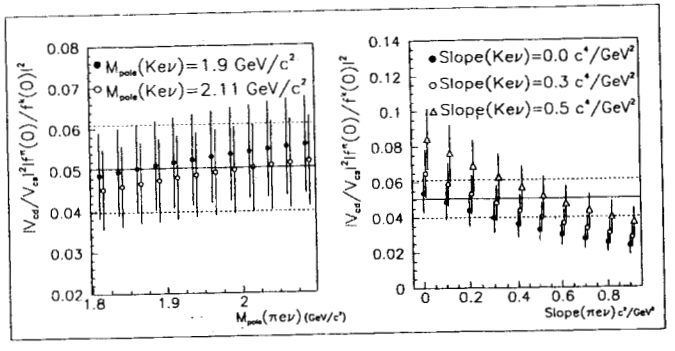

Fig. 47. CKM-ff ratio vs q^2 dependence of f_+^π and f_+^K. (Left) pole and (right) linear. $f_+(q^2) = f_+(0)\ (1 + a\ q^2)$. "Reasonable" choices give $\approx 10\%$ variation.

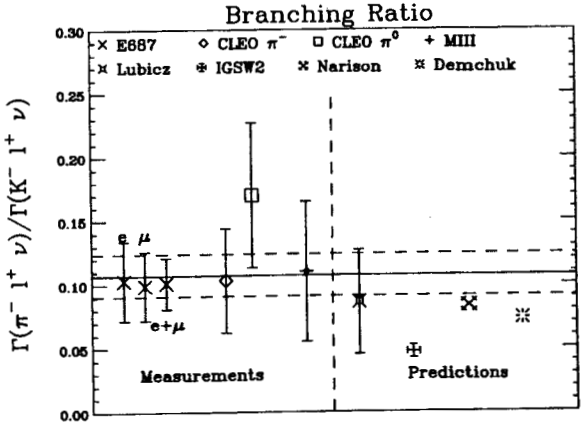

Fig. 48. An informal weighted average gives $\Gamma(\pi^-\ell^+\nu)\,/\Gamma(K^-\ell^+\nu) = 0.11 \pm 0.02$. The data slightly exceeds the predictions.

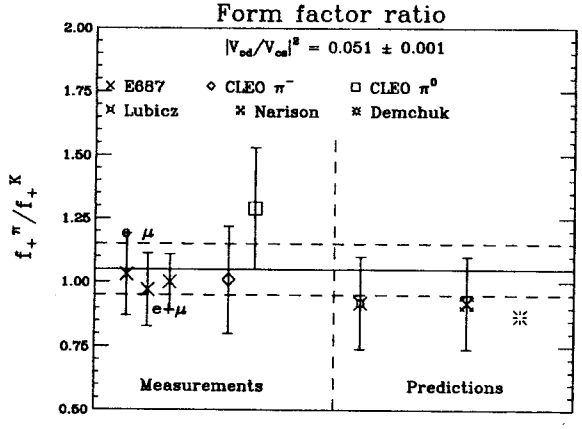

Fig. 49. An informal weighted average of the form-factor ratio is $|f_+^\pi/f_+^k| = 1.05 \pm 0.095$ (assuming $|V_{cd}/V_{cs}|^2 = 0.051$). The predictions are in reasonably good agreement with the prediction.

3.3.4 $D^+ \to K^{*0}\mu^+\nu$

This decay is one of the oldest and cleanest charm semileptonic decays. In fixed-target experiments, one begins with a detached vertex which contains the $K^-\pi^+\mu^+$ charged tracks. As Fig. 50 shows, the $K^-\pi^+$ mass distribution suggests that the four-body decay $D^+ \to K^-\pi^+\mu^+\nu$ is strongly dominated by the quasi-three-body process $D^+ \to K^{*0}\mu^+\nu$. By fitting the $M(K^-\pi^+)$ versus $M(K^-\pi^+\mu^+)$ for the detached events, E687 (Ref. 24) obtained the limit on nonresonant $D^+ \to K^-\pi^+\mu^+\nu$ decays given by Eq. (22),

$$\frac{\Gamma(K^-\pi^+\mu^+\nu)_{\rm nr}}{\Gamma(\{K^-\pi^+\}_{892}\,\mu^+\nu)} = 0.083 \pm 0.029 \;<\; 0.12\ {}_{90\%\ \rm C.L.} \qquad (22)$$

The fact that the $\overline{K^*}$ is a vector particle significantly complicates the Lorentz structure of the weak current $< D^+|J_W|\overline{K^*} >$ which is now described by three q^2 dependent form factors ($A_1(q^2)$ $A_2(q^2)$ $V(q^2)$) (two axial and one vector).** The ratio of the form factors controls the decay angular distribution as illustrated in Fig. 51. Once the R_v and R_2 shape variables are determined, one can measure the overall scale of $A_1(q^2)$ from the decay width in a way highly analogous

**Experimentalists generally analyze their data assuming that the q^2 dependence of these form factors are of the pole form with the D_s^{*+} and D_s^{**+} poles.

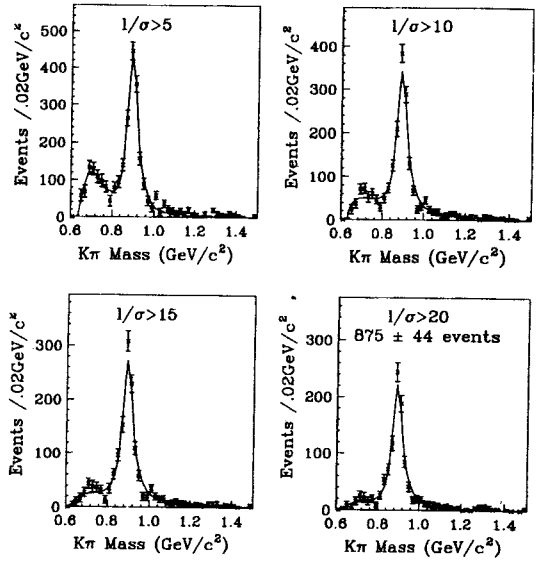

Fig. 50. The subtracted $K^-\pi^+$ invariant mass plot for $D^+ \to K^-\pi^+\mu^+\nu$ events from E687. The right sign–wrong sign subtraction tends to eliminate noncharm background. Increasing the ℓ/σ cut eliminates the low mass $D^{*+} \to (K^-\mu^+\nu)\pi^+$ bump, leaving a $K^-\pi^+$ mass distribution dominated by $\overline{K^*}(892)$.

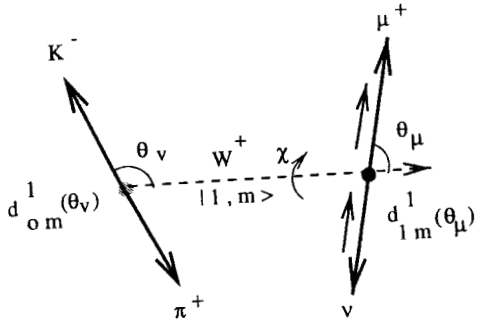

Fig. 51. The three form factors control the q^2 dependence of the virtual W^+ polarization. The spin states of the leptons favored by $V-A$ are shown. The three decay angles are θ_μ describing the virtual $W^+ \to \mu^+\nu$ decay in its rest frame, θ_v describing the $\overline{K^{*0}} \to K^-\pi^+$ in the $\overline{K^*}$ rest frame, and the acoplanarity, χ, between the W and $\overline{K^*}$ decay planes. The decay distribution $d^4\Gamma/\left(d\cos\theta_\mu d\cos\theta_v dq^2 d\chi\right)$ serves to measure $R_v = V(0)/A_1(0)$ and $R_2 = A_2(0)/A_1(0)$.

to the use of Eq. (18). Figures 52 and 53 compare the experimental data to theoretical predictions[26] for both the form factor ratios and $A_1(0)$. Since the initial predictions for the $f_+(q^2)$ form factor which governs $D^o \to K^-\ell^+\nu$ was in good agreement with experimental data, whereas Fig. 53 shows initially the $A_1(q^2)$ which sets the scale of $\Gamma\left(D^+ \to \overline{K^{*o}}\ell^+\nu\right)$ was overpredicted by $\approx \sqrt{2}$, the ratio $\Gamma\left(D_+ \to \overline{K^{*o}}\ell^+\nu\right)/\Gamma\left(D^0 \to K^-\ell^+\nu\right)$ was initially predicted to be a factor of two larger than the measured value of $< \Gamma_{\overline{K^*}\ell\nu}/\Gamma_{\overline{K}\ell\nu} >= 0.56 \pm 0.05$. As Fig. 53 shows, this apparently serious discrepancy with the predictions for A_1 is beginning to fade away as the recent LGT predictions are becoming available. Finally, the recently revised ISGW2 quark model[31] computes $\Gamma_{\overline{K^*}\ell\nu}/\Gamma_{\overline{K}\ell\nu} = 0.54$, which is in excellent agreement with the experimental value.

3.4 Polarization in Charm Baryon Decay

The CLEO and ARGUS Collaborations have studied both semileptonic decay processes such as $\Lambda_c^+ \to \Lambda\ell^+\nu$, and hadronic decay processes such as $\Lambda_c^+ \to \Lambda\pi^+$, and find in either case that the daughter Λ emerges with a spin which is nearly 100% left-handed (when viewed in the Λ_c^+ rest frame). This effect has also been observed in the decays $\Xi_c^o \to \Xi^-\pi^+$. Figure 54 gives an illustration of the effect

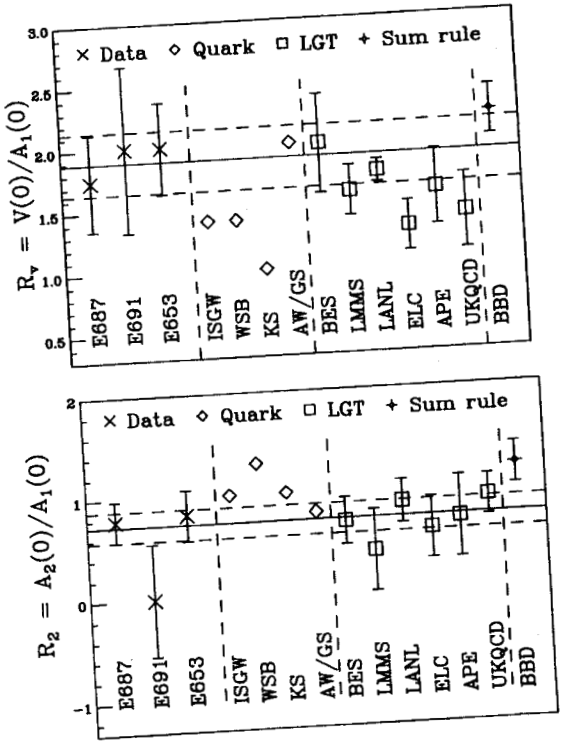

Fig. 52. Experimental averages compared to theoretical prediction for the form factor ratios $R_v = V(0)/A_1(0)$, $R_2 = A_2(0)/A_1(0)$. The horizontal lines give the average of the data. The Lattice Gauge predictions are in good agreement with the data.

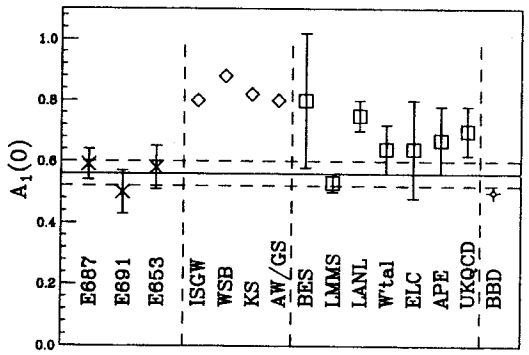

Fig. 53. Experimental averages compared to theoretical predictions for the $A_1(0)$ form factor. The points are in rough chronological order. The earliest quark model points were about 40% higher than the data. The more recent LGT points are in much closer agreement with experiment.

for the case of $\Lambda_c^+ \to \Lambda \ell^+ \nu$ with $\Lambda \to p\pi^-$. The observation of a nearly left-handed daughter baryon in charm decay can be predicted using HQET. Although HQET plays a dramatic role in understanding b-sector physics, to my knowledge, the charmed baryon polarization effect along with the predicted spectroscopy of excited charmed mesons and baryons are the main applications of HQET in the charm sector.

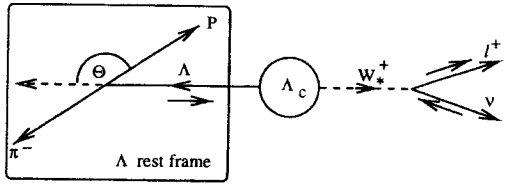

Fig. 54. When viewed in the Λ_c^+ rest frame, the daughter Λ emerges predominantly left-handed, *e.g.*, spinning against its momentum vector. I also indicate the preferred spin directions of the final state leptons in a $V-A$ decay. The Λ can be thought of as self-analyzing in the sense that in the decay $\Lambda \to p\pi^-$, the proton emerges primarily along the Λ spin direction when viewed in the Λ rest frame. See Fig. 55 as well.

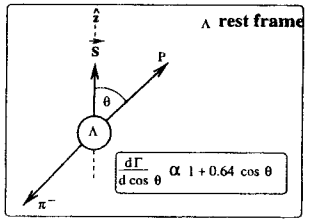

Fig. 55. We view the decay $\Lambda \to p\pi^-$ in the rest frame of a Λ and orientate our $\hat{z}$ axis to be along the Λ spin direction. The polar angle distribution for the proton daughter is of the form $d\Gamma/d\cos\theta \propto 1 + 0.64\cos\theta$. The asymmetry of 0.64 is sometimes called the analyzing power.

We begin by a discussion of the semileptonic decay results. Figure 56 shows the basic semileptonic process. The signature for baryon semileptonic decays is an

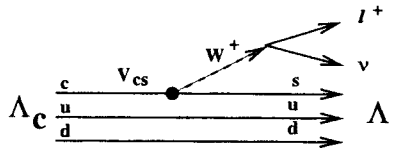

Fig. 56. In the decay $\Lambda_c^+ \to \Lambda \ell^+ \nu$, the daughter baryon is produced along with an ℓ^+ (right sign) rather than an ℓ^- (wrong sign).

excess of right-sign compared to wrong-sign leptons being produced along with the daughter hyperon as illustrated in Fig. 57. One can assign q^2 dependent, helicity form factors for the four ways of assigning spin to the virtual W^+ and daughter Λ which are illustrated by Fig. 58. We can define a Λ polarization asymmetry by Eq. (23). By this definition, $\alpha_{\Lambda_c} = -1$ implies a 100% left-handed daughter Λ.

$$\alpha_{\Lambda_c} = \frac{\Uparrow - \Downarrow}{\Uparrow + \Downarrow} \quad \text{where} \quad \begin{array}{l} \Uparrow \text{means} \vec{S}_\Lambda \parallel \vec{\Lambda} \\ \Downarrow \text{means} \vec{S}_\Lambda \parallel -\vec{\Lambda} \end{array}. \tag{23}$$

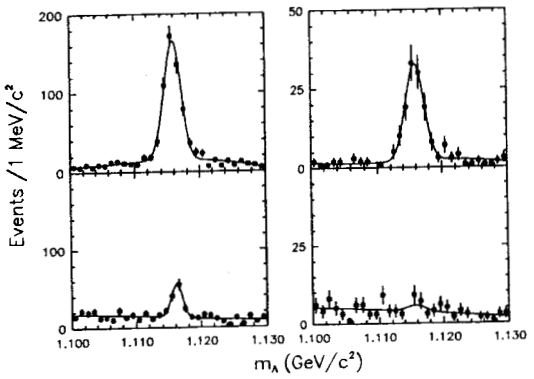

Fig. 57. CLEO right-sign and wrong-sign $\Lambda \to p\pi^-$ signals against an $e^\pm$ (left) or $\mu^\pm$ (right). More $\Lambda\ell^+$ events (top) are seen than $\Lambda\ell^-$ (bottom).

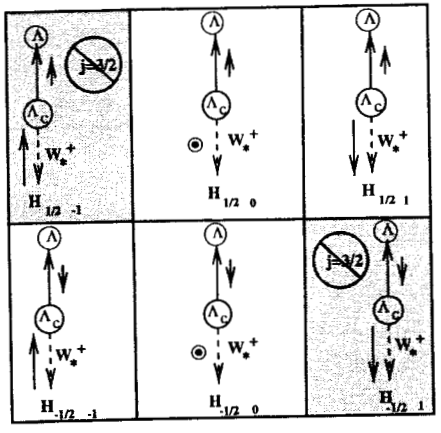

Fig. 58. Four q^2 dependent helicity amplitudes describe this decay. Two of the six possible spin alignments for the spin 1 virtual W^+ and spin 1/2 Λ cannot be produced through the decay of a spin 1/2 Λ_c^+.

Adding together the helicity possibilities shown in Fig. 58, we obtain Eq. (24).

$$\alpha_{\Lambda_c} = \frac{\left(|H^{q^2}_{\frac{1}{2}\,0}|^2 + |H^{q^2}_{\frac{1}{2}\,1}|^2\right) - \left(|H^{q^2}_{-\frac{1}{2}\,-1}|^2 + |H^{q^2}_{-\frac{1}{2}\,0}|^2\right)}{\left(|H^{q^2}_{\frac{1}{2}\,0}|^2 + |H^{q^2}_{\frac{1}{2}\,1}|^2\right) + \left(|H^{q^2}_{-\frac{1}{2}\,-1}|^2 + |H^{q^2}_{-\frac{1}{2}\,0}|^2\right)}. \tag{24}$$

HQET[32] applied to heavy $\to$ light quark transitions such as in charm decay are used to relate these four independent form factors to just two whose ratio $R = f_1/f_2$ controls the q^2 dependence of α_{Λ_c}.†† Angular momentum leads to an additional restriction as $q^2 \to 0$ which is independent of HQET. Figure 59 illustrates the fact that as $q^2 \to 0$, the leptons become collinear and form a spinless system, and only $J_z = 0$ W_*^+'s are formed. In this limit, only two of the four helicity form factors survive this limit. Combining both the angular momentum and HQET restriction, one has the prediction that $\alpha_{\Lambda_c} = -1$ as $q^2 \to 0$, independent of the form factor ratio R. Figure 60 illustrates the predictions of the polarization

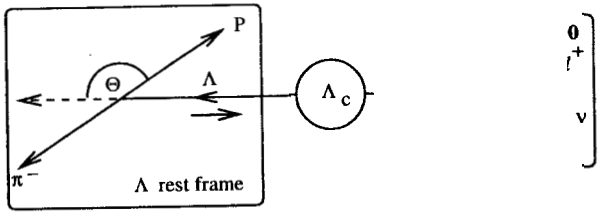

Fig. 59. As $q^2 \to 0$, the ℓ^+ and ν become collinear. By the $V-A$ rules, the neutrino is left-handed and the ℓ^+ becomes right-handed, and their spins cancel. Hence, only $H^{q^2}_{\frac{1}{2}\,0}$, $H^{q^2}_{-\frac{1}{2}\,0} \neq 0$ as $q^2 \to 0$.

asymmetry predicted in the Körner and Krämer model[32] for various values of the form factor ratio R. For the case of heavy $\to$ heavy transitions such as one would get in b-baryon decays, the four form factors are reduced to just one, and thus $\alpha_{\Lambda_b} = -1$ at all q^2.

Rather than going to the $q^2 \to 0$ limit in $\Lambda_c^+ \to \Lambda\ell^+\nu$ decays to form a $J_z(W_*^+) \to 0$, one could directly couple the W_*^+ to a π^+ as illustrated in Fig. 61.

††The two HQET allowed form factors, f_1 and f_2, are generally assumed to have the same q^2 dependence.

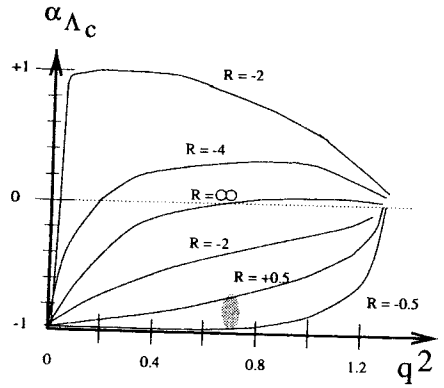

Fig. 60. A crude sketch of the Körner and Krämer predictions for α_{Λ_c} versus q^2 for various form factor ratios. The shaded region is relevant to $\Lambda_c^+ \to \Lambda\ell^+\nu$. Note $\alpha_{\Lambda_c} \to -1$ as $q^2 \to 0$ independent of the form factor ratio R. The basic prediction is that $\alpha_{\Lambda_c} \approx -1$.

Again, for this case of these nonleptonic charm baryon decays, angular momentum conservation combined with HQET applied to heavy $\to$ light transitions predicts a nearly complete left-handed daughter baryon polarization. These results can

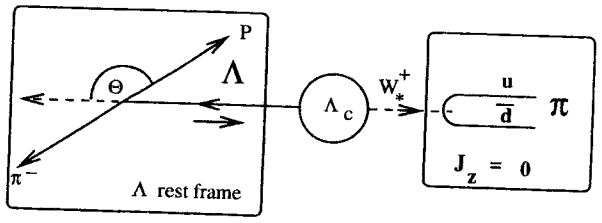

Fig. 61. For $\Lambda_c^+ \to \Lambda\pi_7^+$ $q^2 = m_\pi^2 \to 0$, HQET predicts $\alpha_{\Lambda_c} = -1$.

be extended to the decay $\Xi_c^o \to \Xi^-\pi^+$ where the hyperon daughter subsequently decays via $\Xi^- \to \Lambda\pi^-$. The Ξ^- decay is also self-analyzing with the Λ following a polar angle distribution of the form $(d\Gamma/d\cos\Theta)_\Lambda \propto 1 - 0.46\cos\Theta$. Figures 62 and 63 show acceptance-corrected polar distributions for the $\Lambda \to \underline{p}\pi^-$ and $\Xi^- \to \underline{\Lambda}\pi^-$ from $\Lambda_c^+ \to \Lambda\ell^+\nu$ and $\Xi_c^o \to \Xi^-\pi^+$ decays obtained by the CLEO Collaboration.

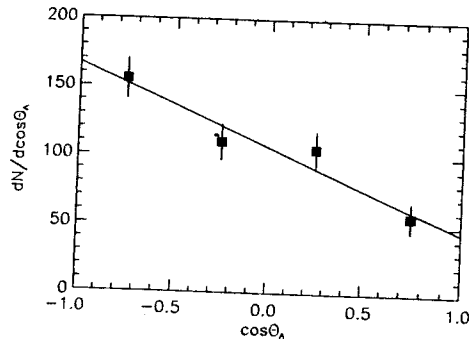

Fig. 62. CLEO's acceptance-corrected measurement of the proton polar angle distribution in the Λ rest frame with respect to the Λ helicity axis for $\Lambda_c^+ \to \Lambda\ell^+\nu$ decays. The Λ helicity axis points against the momentum of the Λ_c^+ when viewed in the Λ rest frame. The slope of this line divided by the Λ analysis power of 0.64 gives $\alpha_{\Lambda_c} \approx -1$.

Figure 64 summarizes the polarization asymmetry obtained for various charmed baryon decay modes. In each case, the asymmetry is consistent with a 100% left-handed polarization as predicted by HQET.

3.5 Nonleptonic Charm Decays

One can profitably study nonleptonic charm decays on several levels. On the most inclusive level, the rough order of magnitude difference between the charm particle lifetimes, discussed in Sec. 3.1, primarily reflects differences in the nonleptonic decay width. The semileptonic width is a small fraction of the total width in the first place, and secondly, although the semileptonic widths of the various charmed particles are not expected to be universal, Table 5 tells us that these widths are expected to be roughly the same.

On the next level of inclusiveness, one can study the partial decay widths of charm mesons into specific two-body final states. Factorization models have been proposed which predict the partial decay widths of two-body decays of charmed

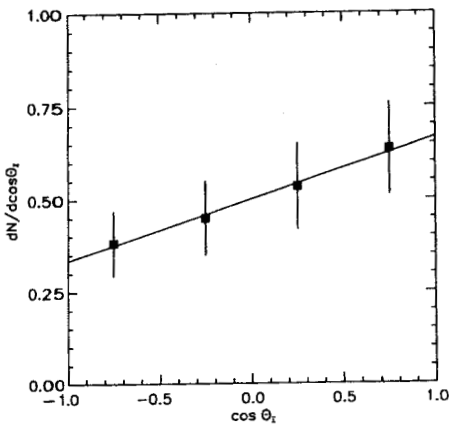

Fig. 63. CLEO's acceptance-corrected measurement of the Λ polar angle distribution in the Ξ^- rest frame with respect to the Ξ^- helicity axis in $\Xi_c^o \to \Xi^-\pi^+$ decays. The slope of this line divided by the Ξ^- analysis power of -0.46 gives $\alpha_{\Xi_c^o} \approx -1$.

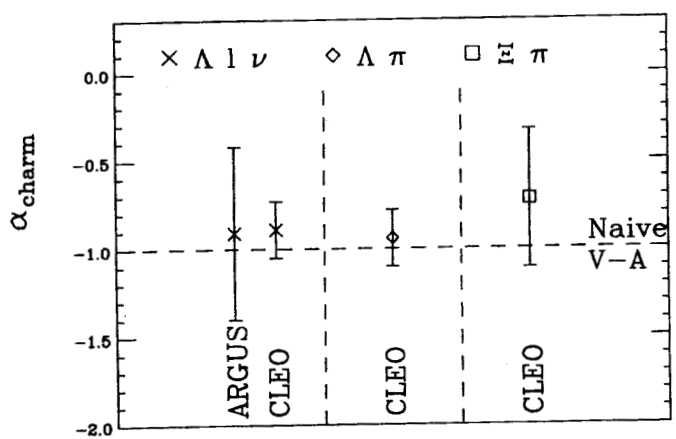

Fig. 64. The polarization asymmetry of the daughter hyperon observed for the charmed baryon decays studied thus far. The horizontal dashed line gives the $V-A$ left-handed helicity predicted by HQET.

mesons in the absence of final-state interactions. Final-state interaction effects become apparent in the interference between the various isospin amplitudes which contribute to different charged variants of a given final state. The simplest experimental tests of factorization involve pure two-body decays of charmed mesons into two pseudoscalar final states involving kaons and pions.

One can extend factorization tests to quasi-two-body decays such as pseudoscalar-vector decays as well as vector-vector decays by analyzing the resonance structure in multibody, nonleptonic, charmed meson decays. Experience has shown that the data is best fit by models where the various resonant channels contribute coherently to a decay amplitude, and thus, interfere in the differential decay width. These amplitude analyses provide additional handles on final-state interaction effects through interference of the amplitudes describing competing resonant channels in, *e.g.*, a three-particle decay Dalitz plot.

The factorization framework, in which nonleptonic charm decays have been traditionally analyzed, begins with an effective Hamiltonian such as that given by Eq. (25) describing CKM-allowed decays:

$$\mathcal{H} = \frac{G_f}{\sqrt{2}} V_{cs}^* V_{ud} \left(\frac{C_+ + C_-}{2} (\bar{u}\, d)\, (\bar{s}\, c\,) + \frac{C_+ - C_-}{2} (\bar{s}\, d)\, (\bar{u}\, c) \right). \qquad (25)$$

The Hamiltonian of Eq. (25) incorporates QCD corrections to the underlying weak decay process through the use of renormalization group methods. The coefficients $C_\pm$ are called "Wilson coefficients." In the absence of QCD corrections, $C_+ = C_-$, and one recovers a single weak process corresponding to the familiar spectator diagram of Fig. 65. The Wilson coefficients depend on the scale of the QCD-coupling

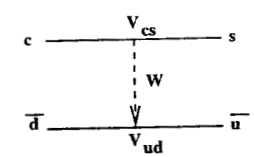

Fig. 65. When $C_+ = C_-$, the second term of Eq. (25) disappears, and one has the CKM spectator diagram.

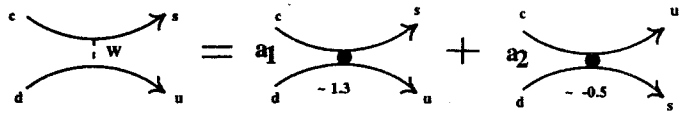

Fig. 66. The effective charged current whose amplitude $a_1 \approx (C_+ + C_-)/2$ (with a small color correction) describes the familiar spectator process. The effective neutral current process, with an amplitude $a_2 \approx (C_+ - C_-)/2$ which decreases as $M_Q \to \infty$, gives rise to nonspectator effects which are important in charm but less so in beauty.

constants. When taken at the charmed quark mass, the Wilson coefficients have the values given by Eq. (26)

$$\frac{C_+(M_Q) + C_-(M_Q)}{2} \approx 1.25\,, \quad \frac{C_+(M_Q) - C_-(M_Q)}{2} \approx -0.49. \qquad (26)$$

In 1987, Bauer, Stech, and Wirbel (BSW)[33] combined these ideas into an explicit model which applied two-body and quasi-two-body nonleptonic charmed meson decay. In the BSW model, the two terms of Eq. (25) are organized into an effective "charged" current and effective "neutral current" between the parent and daughter hadrons as illustrated in Fig. 66. If a given nonleptonic charm decay can only proceed through the effective charged current interaction, it is classified as a Class 1 process. Class 2 processes only proceed through the effective neutral current interactions. Class 3 processes have contributions from both interactions. In the process, $D^o \to K^-\pi^+$, illustrated by Fig. 67, one has a neutral parent and two charged daughters, and hence, this must be a Class 1 process. In the Class 2 process, $D^o \to \overline{K^o}\pi^o$, illustrated by Fig. 68, one has neutral parent D^o decaying into two neutral daughters. The CKM-allowed decays of the D^+ such as $D^+ \to \overline{K^o}\pi^+$, depicted in Fig. 69, are Class 3 processes.

According to the Watson theorem, the weak amplitudes predicted in factorization models such as BSW must all be relatively real. However, the final-state hadrons can continue to interact via long-range strong interactions and acquire complex phases. These final state interactions (FSI) can be accommodated by multiplying the bare (weak) amplitudes by the square root of a complex, unitary S matrix describing the strong rescattering. To illustrate the effects of FSI,

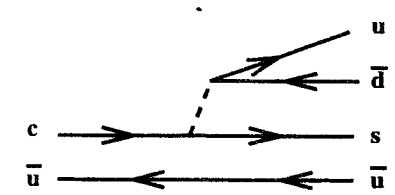

Fig. 67. In the BSW model, the amplitude for this decay is written as $a_1\ G_f\ 2^{-1/2}\ < \pi^+|(\bar{u}d)|0 >< K^-|(\bar{s}c)|D^o >= a_1\ G_f\ 2^{-1/2}\ (-if_\pi P_\pi) \times f_+(m_\pi^2)$. The coupling of the π^+ with respect to the virtual W^+ involves the same current as the leptonic decay $\pi^+ \to \ell^+\nu$ which is proportional to the pion-lepton decay constant. The CKM-allowed current which describes the process $D^o \to W^{+*}\ K^-$ is the same current involved in the semileptonic decay process $D^o \to K^-\ell^+\nu$ which is described by the form factor $f_+(q^2)$.

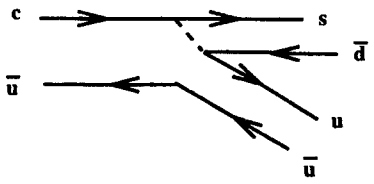

Fig. 68. In the BSW model, the amplitude for this decay is written as $a_2\ G_f\ 2^{-1/2}\ < \overline{K^o}|(\bar{s}d)|0 >< \pi^o|(\bar{u}c)|D^o >$ where again the currents involve the leptonic and semileptonic form factors. Note that the light $\bar{u}$ constituent of the D^o does not spectate as is the case in Fig. 67, but is actively rearranged into the final-state hadron.

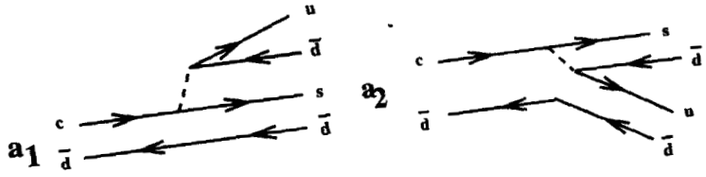

Fig. 69. The two processes depicted in the figure differ by the exchange of $\bar{d}$ quark fermion in the final state. Because a_1 and a_2 interfere with the opposite sign, one generally has destructive interference for D^+ decays which causes the D^+ to have a longer life than the D^o.

consider the isospin classification of three amplitudes related to $D \to \pi\pi$ decay:

$$A(D^o \to \pi^-\pi^+) = \frac{1}{\sqrt{3}}\left(\sqrt{2}\, a_o + a_2\right)$$

$$A(D^o \to \pi^o\pi^o) = \frac{1}{\sqrt{3}}\left(-a_o + \sqrt{2}\, a_2\right) \quad , \quad A(D^+ \to \pi^o\pi^+) = \sqrt{\frac{3}{2}}\, a_2. \tag{27}$$

The measured a_o and a_2 amplitudes will acquire complex phases through the FSI S matrix as indicated in Eq. (28)

$$\begin{pmatrix} a_0 \\ a_2 \end{pmatrix} = \begin{pmatrix} \eta\, e^{2i\delta_0} & \cdot\; i\sqrt{1-\eta^2}\, e^{i(\delta_0+\delta_2)} \\ i\sqrt{1-\eta^2}\, e^{i(\delta_0+\delta_2)} & \eta\, e^{2i\delta_2} \end{pmatrix}^{1/2} \begin{pmatrix} a_0 \\ a_2 \end{pmatrix}_{\text{bare}} . \tag{28}$$

Since QCD respects isospin symmetry, there should be no mixing between a_o and a_2, which means the elasticity parameter in Eq. (28) should be $\eta = 1$.‡‡ Even a purely elastic FSI can change the total width of charm decays into a particular final state by changing the value of $\cos(\delta_2 - \delta_0)$ when converting, *e.g.*, $A(D^o \to \pi^-\pi^+)$ into $\Gamma(D^o \to \pi^-\pi^+)$ via Eq. (29)

$$\Gamma(\pi^+\pi^-) = \frac{2}{3}\,|a_o|^2 + \frac{1}{3}\,|a_2|^2 + \frac{2\sqrt{2}}{3}|a_o|\,|a_2|\,\cos(\delta_2 - \delta_0). \tag{29}$$

‡‡One can still have, however, inelastic final state interactions between final states such as $D \to \pi\pi$ and $D \to KK$ since a dipion final state can potentially scatter into a dikaon final state. One could accommodate such a case with a 4×4 matrix describing the two isospin amplitudes for the dipion and two isospin amplitudes for the dikaon.

The unexpectedly large branching ratio for the decay $D^o \to K^+K^-/\pi^+\pi^-$ provided an early example of the possible role of FSI affecting branching ratios. Table 7 summarizes recent data on $\Gamma(K^+K^-)/\Gamma(\pi^+\pi^-)$. As one can see from

Table 7. $\Gamma(D^o \to K^+K^-)/\Gamma(D^o \to \pi^+\pi^-)$.

E687 (Ref. 34)	WA82 (Ref. 35)
$2.53 \pm 0.46 \pm 0.19$	$2.23 \pm 0.81 \pm 0.46$
E691 (Ref. 36)	CLEO (Ref. 37)
$1.95 \pm 0.34 \pm 0.22$	$2.35 \pm 0.37 \pm 0.28$

Table 7, although both processes are CKM suppressed by the same amount and $D^o \to \pi^+\pi^-$ is favored by having a larger phase space, $D^o \to K^+K^-$ occurs at roughly twice the rate as $D^o \to \pi^+\pi^-$. Since these decays were the first CKM-suppressed decays to be studied, their width ratio was initially quite surprising. In the context of the BSW model, both decays are Class 1 processes, since no effective neutral currents are possible between the parent and either daughter, and the BSW model makes the prediction $\Gamma(K^+K^-)/\Gamma(\pi^+\pi^-) \approx 1.4$ independent of the Class 2 normalization. Conventional wisdom has it that discrepancy between the data and the BSW prediction is due to FSI changing the phase of interfering dipion or dikaon isospin amplitudes.

A more direct way of seeing the effects of final-state interactions is to measure the widths into various isospin-related channels such as $\Gamma(\pi^+\pi^-)$, $\Gamma(\pi^o\pi^o)$, and $\Gamma(\pi^+\pi^o)$, and extract a_0, a_2, and $\cos(\delta_2 - \delta_0)$ by solving Eq. (29) and the two similar equations. Table 8 taken from the upcoming ***Annual Review*** article by Pedrini, Browder, and Honschied[38] summarizes the results of such isospin analyses for many two-body and quasi-two-body charm decays. Table 8 shows that more often than not, a considerable phase shift is observed between the two isospin amplitudes. Watson's theorem tells us that phase shifts between interfering isospin amplitudes where $\sin(\delta_{I'} - \delta_I) \neq 0$ cannot arise from the weak processes alone and thus constitute direct evidence for FSI.

Several groups[40-43] have gone a step further and published resonant amplitude analyses of particular final states. Most of this work concerns three-body decays where all of the amplitude information resides in the Dalitz plot. Amplitude analyses allow one to extend factorization model tests to pseudoscalar-vector

Table 8. Isospin amplitude ratios and phase shifts for two-body charm decays.

Mode	Ratio of amplitudes	$\delta = \delta_I - \delta_{I'}$
$K\pi$	$\lvert A_{1/2}\rvert/\lvert A_{3/2}\rvert = 4.12 \pm 0.40$	$88° \pm 8°$
$K^*\pi$	$\lvert A_{1/2}\rvert/\lvert A_{3/2}\rvert = 5.23 \pm 0.59$	$90° \pm 16°$
$K\rho$	$\lvert A_{1/2}\rvert/\lvert A_{3/2}\rvert = 3.22 \pm 0.64$	$10° \pm 47°$
$K^*\rho$	$\lvert A_{1/2}\rvert/\lvert A_{3/2}\rvert = 4.93 \pm 1.95$	$33° \pm 57°$
KK	$\lvert A_1\rvert/\lvert A_0\rvert = 0.58 \pm 0.12$	$47° \pm 13°$
$\pi\pi$	$\lvert A_2\rvert/\lvert A_0\rvert = 0.63 \pm 0.13$	$81° \pm 10°$

and vector-vector nonleptonic decays of D mesons and provide new ways of studying FSI effects. A particularly clean and instructive example is provided by the E687 (Ref. 43) group's analysis of the $D^+, D_s^+ \to K^-K^+\pi^+$ final state. Mass histograms and the two Dalitz plots are shown in Fig. 70.

The D_s^+ Dalitz plot is dominated by the $\phi\pi^+$ and $\overline{K}^{0*}K^+$ channels, while the D^+ also has a significant contribution from a single or multiple broad resonances. We note that both the ϕ and $\overline{K}^*$ bands have a node due to angular momentum conservation in the center of each band as illustrated in Fig. 71. In order to extract information from Dalitz plots such as those illustrated in Fig. 70, the experimental groups fit the intensity across a Dalitz plot to a coherent sum of quasi-two-body or possible nonresonant contributions. For example, one can fit the D_s^+ Dalitz plot to the form $d^2\Gamma/(dM_1^2 dM_2^2) \propto |\mathcal{A}(D_s^+ \to K^+K^-\pi^+)|^2$, where the amplitude is given by Eq. (30)

$$\mathcal{A}(D_s^+ \to K^+K^-\pi^+) = a_{\overline{K}^*}\, e^{i\delta_{\overline{K}^*}} \mathcal{M}(\pi^+K^-K^+|\overline{K^{*0}}\,K^+) + a_\phi\, e^{i\delta_\phi} \mathcal{M}(K^+K^-\pi^+|\phi\pi^+) + \ldots . \quad (30)$$

Figure 72 illustrates the form of one of these quasi-two-body contributions. Each resonant channel contribution is multiplied by a complex amplitude coefficient whose modulus serves as a gauge to the relative "importance" of the channel.*

*In fitting to the shape of the relative event density across the Dalitz plot, one of the fitted amplitude factors is generally set to unity and serves as a reference channel. Clearly, since one is fitting to $|\mathcal{A}|^2$, the overall phase of $\mathcal{A}$ cannot be measured. The modulus of the reference amplitude can be determined if desired through the total decay width in a way similar in spirit to Eq. (18).

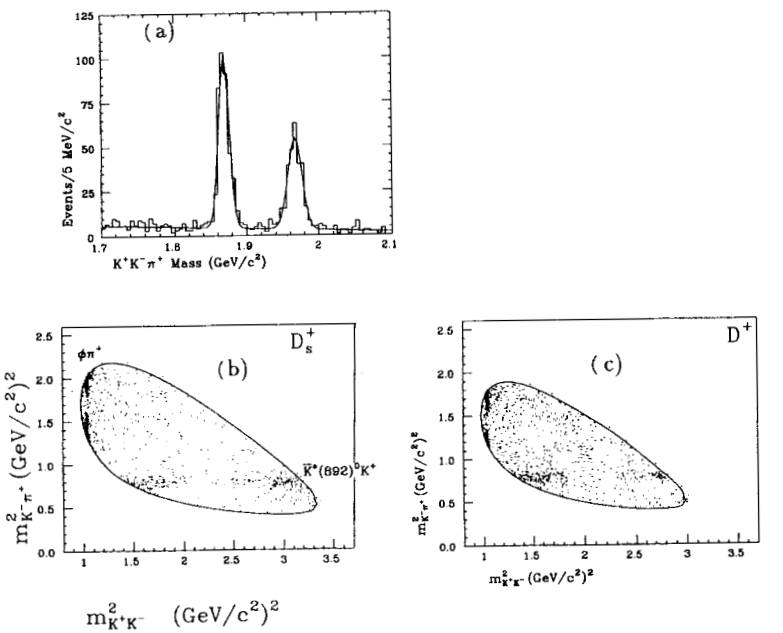

Fig. 70. (a) The mass spectrum for out-of-target $K^+K^-\pi^+$ decays. (b) and (c) The full sample $D_s^+, D^+ \to K^-K^+\pi^+$ Dalitz plots. The bands due to $\overline{K^{*0}}(890)K^+$ and $\phi(1019)\pi^+$ are quite visible for both the D_s^+ and D^+ Dalitz plots. Note the significant asymmetry between the population of the high and low $\overline{K^{*0}}(890)K^+$ lobes for the D^+ in sharp contrast with the symmetric appearance of the lobes for the D_s^+.

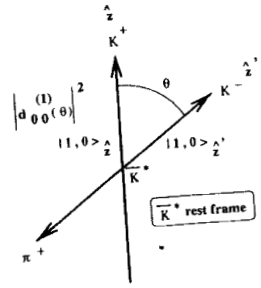

Fig. 71. When viewed in the $\overline{K^*}$ rest frame, the $\overline{K^*}$ has zero spin along the $\overline{K^*} \to K^-\pi^+$ decay axis since neither decay product carries spin. Since the D and D^+ are both spinless, the $\overline{K^*}$ must have zero spin along the K^+ axis. The amplitude for the $\overline{K^*}$ to have been in these two simultaneous spin states is given by $d^{(1)}_{00}(\theta) \propto \cos\theta$. This angular factor causes the Dalitz intensity to vanish in the center of the Dalitz band where $\cos\theta = 0$ as discussed in Fig. 25.

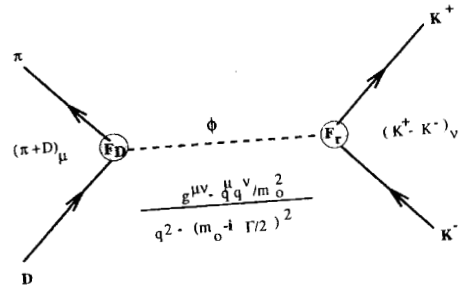

Fig. 72. We show a Feynman-like diagram for the process $D_s^+ \to \phi\pi^+$. A $D \to \pi^+$ current with a form factor F_D interacts with a kaon current with form factor F_r through an unstable ϕ propagator with an imaginary width contribution to the propagator mass. This diagram gives an amplitude contribution of the form $\mathcal{M} = F_D\, F_r \times |\vec{c}|^J |\vec{a}|^J P_J(\cos\theta^r_{ac}) \times BW(m_{ab})$, where the angular factor which gives rise to the Dalitz nodes follows from the structure of current × current contribution, and the Breit-Wigner represents the unstable propagator. The form factors are relatively unimportant.

Any nonreal phase differences are due to the influence of final state interactions which in a two resonant model would be given by Eq. (31)

$$\begin{pmatrix} a_{\overline{K}^*}\, e^{i\delta_{\overline{K}^*}} \\ a_\phi\, e^{i\delta_\phi} \end{pmatrix} = \begin{pmatrix} \eta\, e^{2i\delta_1} & i\sqrt{1-\eta^2}e^{i(\delta_1+\delta_2)} \\ i\sqrt{1-\eta^2}e^{i(\delta_1+\delta_2)} & \eta\, e^{2i\delta_2} \end{pmatrix}^{1/2} \begin{pmatrix} a_{K^*} \\ a_\phi \end{pmatrix}_{\text{bare}} . \tag{31}$$

One of the more interesting features of the Dalitz plots of Fig. 70 is the pronounced asymmetry between the two $\overline{K^*}$ lobes for the $D^+ \to K^-K^+\pi^+$. We believe that this lobe asymmetry is due to interference of the $\overline{K^{*0}}K^+$ channel with a broad, spinless resonance channel. From the interference pattern, one can infer that the data requires a nearly imaginary relative phase shift. For simplicity, we model the broad resonance in the vicinity of the $\overline{K^*}$ as a nearly constant amplitude which we write as $\cos\,\delta + i\sin\,\delta$. Equation (32) gives an explicit form for this interference term

$$Re\left\{(\cos\,\delta + i\sin\,\delta)^* \,\frac{\cos\,\theta}{M_r^2 - M_{K\pi}^2 - i\Gamma M_r}\right\} = \frac{(M_r^2 - M_{K\pi}^2)\,\cos\,\theta\,\cos\,\delta}{(M_r^2 - M_{K\pi}^2)^2 + \Gamma^2 M_r^2} + \frac{\Gamma M_r\,\cos\,\theta\,\sin\,\delta}{(M_r^2 - M_{K\pi}^2)^2 + \Gamma^2 M_r^2}. \tag{32}$$

The asymmetry comes about because the $\overline{K^{o*}}K^+$ decay amplitude contains an angular factor of $\cos\theta$, where θ is the angle between the two kaons in the $\overline{K^{o*}}$ rest frame. This $\cos\theta$ factor causes the interference term to change sign from the left lobe to the right lobe. We get an interference term from both the real part of the Breit-Wigner as well as the imaginary part. Since the real part of a Breit-Wigner reverses sign as one passes through the resonance (thus canceling the net interference across the lobe), any net interference is due to the second term which is proportional to $\sin\delta$. Figure 73 makes this argument graphically. The net lobe asymmetry thus provides visible evidence for final-state interactions since all bare amplitudes must be real ($\delta = 0$ or 180°). After exploring many possibilities, E687 settled on the $\overline{K_0^*}(1430)$ K^+ channel as the most likely channel interfering with the $\overline{K^{*0}}K^+$ band.

We next discuss the $D_s^+ \to K^+K^-\pi^+$ Dalitz plot. A close examination of the Dalitz plot for the nearly background-free, out-of-target data (Fig. 74) shows an accumulation of events in (what should be) the ϕ band angular node. E691 (Ref. 44) discovered that the $D_s^+ \to \pi^+\pi^-\pi^+$ Dalitz plot is strongly dominated by the channel $D_s^+ \to f(980)\pi^+ \to (\pi^+\pi^-)\pi^+$. We therefore expect a contribution from the known dikaon decay of the $f(980)$ which should populate the ϕ node

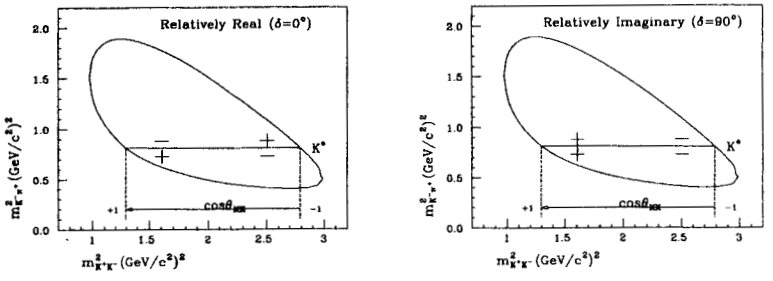

Fig. 73. The "+" and "−" indicate the sign of the interference term between a constant phase and the $\overline{K^{o*}}K^+$ Dalitz band for the case of relatively real (left) and relatively imaginary (right) phase shift. The sign alternates from the left to the right of the band owing to the $\cos\theta$ portion of the $\overline{K^{o*}}$ amplitude in Eq. (32). The real part of a Breit-Wigner amplitude reverses sign as one passes through the resonance which implies an additional sign change for the relatively real case. The relatively imaginary part has no such additional sign reversal.

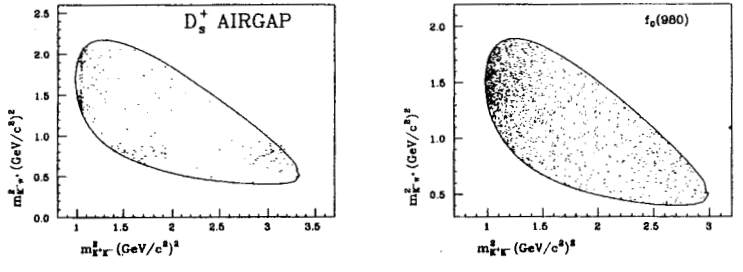

Fig. 74. The E687 D_s^+ Dalitz plot, and simulated $D_s^+ \to f(980)\pi^+ \to (K^+K^-)\pi^+$ decays.

region as shown in Fig. 74. Figure 75 shows us that the inclusion of additional contributions from the $f_J(1710)\pi^+$ and $\overline{K_0^*}(1430)\ K^+$ significantly improved the quality of the fits in the vicinity of the K^* peak (R_1) and just above it (R_2).

Table 9 compares the E687 (Ref. 43) results on the channels common to both the $D^+, D_s^+ \to K^+K^-\pi^+$decays. The fractions, f_r, are known as decay fractions and represent the ratio of the integrated Dalitz intensity for a single resonance r divided by the intensity with all contributions present. The D^+ amplitude consists of nearly equal contributions of $\overline{K^*}K$, $\phi\pi$, and $\overline{K^*}(1430)^0K^+$; while the D_s^+ is strongly dominated by just the $\overline{K^*}K$ and $\phi\pi$. The decay fraction for the $f_o(980)$ and $f_J(1710)$ contributions to the D_s^+ sum to 14%.†

Table 9. Comparison of $D^+, D_s^+ \to K^+K^-\pi$ amplitudes.

Parameter	D^+	D_s^+
$\delta_{\overline{K}^*(892)^0K+}$	0^o (fixed)	0^o (fixed)
$\delta_{\phi\pi^+}$	$-159 \pm 8 \pm 11^o$	$178 \pm 20 \pm 24^o$
$\delta_{\overline{K}^*(1430)^0K+}$	$70 \pm 7 \pm 4^o$	$152 \pm 40 \pm 39^o$
$f_{\overline{K}^*(892)^0K+}$	$0.301 \pm 0.020 \pm 0.025$	$0.478 \pm 0.046 \pm 0.040$
$f_{\phi\pi^+}$	$0.292 \pm 0.031 \pm 0.030$	$0.396 \pm 0.033 \pm 0.047$
$f_{\overline{K}^*(1430)^0K+}$	$0.370 \pm 0.035 \pm 0.018$	$0.093 \pm 0.032 \pm 0.032$

Both the D^+ and D_s^+ could be fit entirely by quasi-two-body processes without the need to include a nonresonant contribution. It is interesting to note that both charm states have a real relative phase between the dominant $\overline{K^*}K$ and $\phi\pi$ channels which indicates absent or canceling FSI phase shifts.

Our amplitude fit for $D^+ \to K^-K^+\pi^+$ enables us to correct for acceptance variations across the Dalitz plot as well as the effects of resonant channel interference to obtain a much improved inclusive branching ratio $D^+ \to K^+K^-\pi^+/K^-\pi^+\pi^+ = 0.0976 \pm 0.0042 \pm 0.0046$. It has become common practice to quote "branching ratios" for resonant decay amplitudes such as $D^+ \to \phi\pi^+/K^-\pi^+\pi^+$, but because of quantum mechanical interference, only such inclusive ratios as $D^+ \to K^+K^-\pi^+/K^-\pi^+\pi^+$ are truly legitimate.

†I find it interesting to note that both the $f_o(980)$ and $f_J(1710)$ are often suspected to be non-$q\bar{q}$ states. There is a discussion of this in the 1996 summary by the Particle Data Group.[45]

Several groups have performed Dalitz analyses for the $D^o, D^+ \to K\pi\pi$ final state. Although these fits provide a good qualitative match to the data, often discrepancies are apparent in comparisons between the data and mass projections as shown in Fig. 76. The fit fractions obtained by the various experiments[46–48] are in excellent agreement; while there is little agreement concerning the relative phases, as illustrated in Fig. 77 for $D^o \to K^o_s\pi^+\pi^-$. There is excellent agreement, however, between phases obtained by E687 (Ref. 46) and Argus.[48] These analyses provide a wealth of information on new decay modes which can be compared to models based on factorization, QCD sum rules, and $1/N_c$ expansions. Generally, agreement of the models with the data is only at about the ± 60 % level. Often, the isospin amplitudes show nearly imaginary relative phases as reported in Table 8. It is interesting to note that all experimental groups report a sizable nonresonant contribution to the $D^+ \to K^-\pi^+\pi^+$ Dalitz plot which makes it unique among the plots discussed here.

3.6 Heavy Quark Decay Summary

Here is a very brief summary of this rather lengthy section. We began by discussing charm decay at the most inclusive level—the total decay rate or inverse lifetime of the charmed particles. The lifetime of the last measured weakly decaying charmed baryon, the Ω_c^o (css) (2704) state, was measured last year at 0.064 ± 0.020 ps. There is approximately an order of magnitude difference in the lifetime of the short-lived Ω_c^o (css) (2704) state and the long-lived (1.06 ps) D^+. In the absence of QCD effects, the naive spectator model predicts a universal charm lifetime of ≈ 0.7 ps. Recent progress in $1/M_Q$ expansions provides a systematic approach to estimating the effects of WA, WX, and PI diagrams which differentiate among the various charm particle species. The expansion approach does a credible job of reproducing observed lifetimes of the seven known weakly decaying charm states. By way of contrast, the lifetimes of the weakly decaying beauty states are much closer in value. More precise charm baryon measurements and b-sector measurements are needed to fully test these promising new approaches.

HQET predicts a very strong, backward polarization for the daughter baryon in $\Lambda_c \to \Lambda\ell\nu$, such as $\Lambda_c \to \Lambda\pi$, and $\Xi_c \to \Xi\pi$. The spin of the baryons are

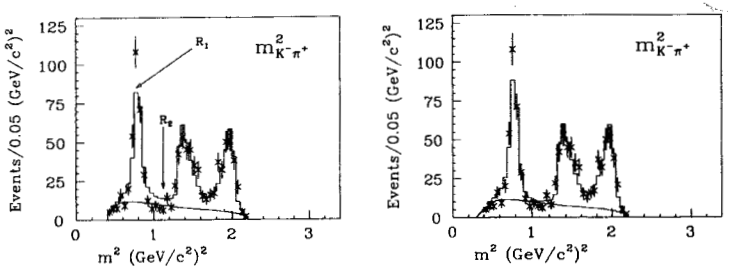

Fig. 75. Comparing the $m^2(K^-\pi^+)$ three amplitude (left) and five amplitude (right) D_s^+ fit to the data (error bars). The background, deduced from the mass sidebands, is shown in the lower histogram.

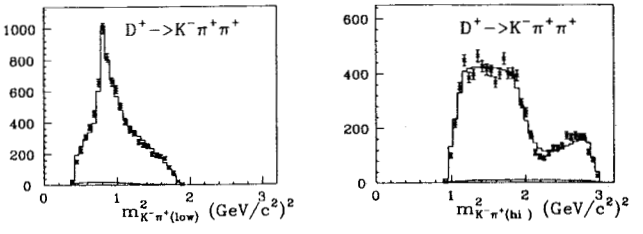

Fig. 76. Comparison of the lower and higher $K^-\pi^+$ mass projection in E687 data (error bars) and our fit (histogram). The high projection does not match near 2.5 GeV^2.

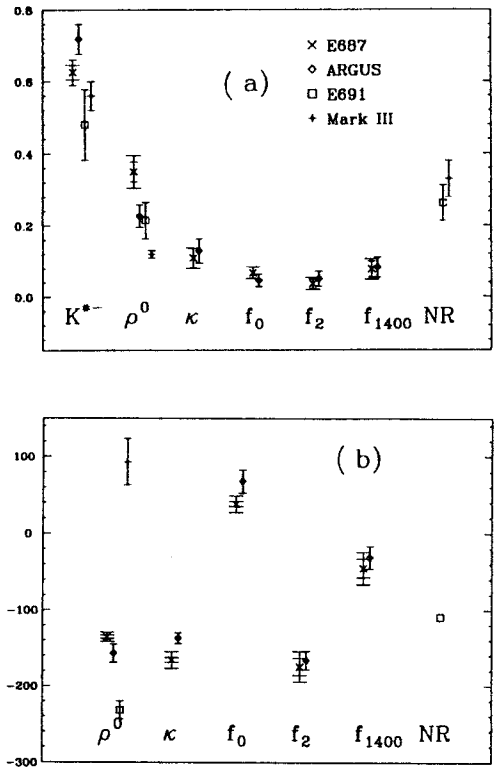

Fig. 77. Comparison of (a) the decay fractions and (b) phases obtained by different experiments for the decay $D^o \to K^o_s\pi^+\pi^-$.

self-analyzed through the decays: $\Lambda \to p\pi$ and $\Xi \to \Lambda\pi$. All three decays were measured by ARGUS and/or CLEO and found to be consistent with nearly complete, left-handed polarization.

A great deal of progress has been made in leptonic and semileptonic decays. There now exist several measurements of the $D_s^+ \to \mu^+\nu$ decay constant. Present data is internally consistent with a value of $f_{D_s} = 242 \pm 32\ MeV$ at $\approx 20\%$ CL level. This value is in good agreement with many of the predictions from Lattice Gauge Theory.

Charm form factors are exactly computable (in principle) by Lattice Gauge Theory and are frequently estimated by Quark Models. Both techniques are most effective when the daughter hadron is at rest relative to the parent, which means that they work best at $q^2 \approx q^2_{\rm max}$. Both the phase space and $V-A$ matrix element tend to force the data to values close to $q^2 \approx 0$. Most experimental groups use a VDM-inspired pole form to bridge the experimental and theoretical q^2 regimes, where the pole mass corresponds to the known D^* and D^{**} spectroscopy. The validity of these forms is unproven.

Theory does a good job predicting the f_+ form factor for $D \to K\ell\nu$. Data favors an $m_{\rm pole}$ slightly lower than the expected D_s^* mass. Crude experimental information on the lepton mass suppressed form factor, $f_-(q^2)$, has just become available. As expected, f_+^π for $D \to \pi\ell\nu$ is equal (to within $\pm 10\%$) to f_+^K for $D \to K\ell\nu$. Since $\pi\ell\nu$ probes q^2 much closer to the pole mass, pole mass uncertainty is an important source of systematics on the form factor and branching ratio measurements. It will be exciting to measure the q^2 dependence of $\pi\ell\nu$ decay in the future. Recent LGT and improved QM calculations are in much better agreement with the form factor magnitude in $D \to \overline{K^*}\ell\nu$ decay than the first predictions.

A factorization framework, the Bauer-Stech-Wirbel (BSW) model, was designed to incorporate QCD corrections into nonleptonic decays. The BSW model deals specifically with two-body and quasi-two-body decays. Predictions are made in terms of leptonic and semileptonic form factors. It has been known for some time that long-range, final-state interactions, FSI, can significantly distort BSW predictions for two-body-decay branching ratios. FSI is also responsible for creating complex phase shifts between isospin amplitudes. Amplitude analyses have confirmed the quasi-two-body nature of most three-body decays. FSI effects are evident in the interference between resonant channels. Amplitude analyses make possible vector-vector, and vector-pseudoscalar comparisons with the BSW model.

Only ±60% agreement exists between the models and resonance data. Extending these analyses to higher multiplicity meson and baryon decays and improving the physics of nonresonant terms is a future goal of charm physics.

4 A Final Word

I have tried throughout these lectures to capture some of the excitement of the present research on charm quark production and decay. Charm provides a unique window to test the calculations of QCD which is in many respects complementary to beauty owing to its intermediate mass scale. Charm lies somewhere between the light quark chiral limit and the limit where HQET is clearly applicable.

I have tried to show that the charm quark appears to be massive enough such that data on high-energy charm photoproduction and hadroproduction cross sections can be reasonably compared to the perturbative QCD calculations at next-to-leading order. The smaller mass of charm compared to beauty offers the experimentalist two distinct advantages. The low mass means that charm is copiously produced in high-energy fixed-target experiments. The reduced decay phase space of charm compared to beauty means that there exist easily reconstructible final states with appreciable ($\approx$ 5–10%) branching fractions. A copious sample of reconstructed charm decays allows one to make rather incisive tests of the QCD production mechanism and fragmentation models involving high-accuracy measurements of particle–antiparticle asymmetries and correlations.

Nonperturbative models have been successfully employed in understanding both the overall decay rate and details concerning form factors for both fully leptonic and semileptonic decays. The emerging calculational tool for charm decay appears to be Lattice Gauge theory since charm semileptonic decays are generally not in the proper domain of HQET. There still remains the problem of the q^2 gulf between where data exists and where the theories work best. Finally, many of the attempts to understand the bulk of charm decay--nonleptonic decay—are presently thwarted by the difficult-to-compute influence of final-state interactions. The final-state interactions will ultimately complicate future beauty physics, but at a hopefully reduced level. When viewed in this context, charm nonleptonic decay perhaps provides a "preview of coming distractions" for future beauty physics.

I would like to acknowledge the hospitality of the SLAC Summer Institute for arranging and maintaining this excellent school and conference. I would also like to acknowledge the prodigious efforts of my many E687 collaborators over the years.

References

[1] E687 Collaboration, P. L. Frabetti *et al.*, Nucl. Instrum. Methods, Phys. Res. Sec., A **320**, 519 (1992).

[2] Mark I Collaboration, G. Goldhaber *et al.*, Phys. Rev. Lett. **37**, 255 (1976).

[3] S. Frixione, M. Mangano, P. Nason, and G. Ridolfi, Nucl. Phys. B **405**, 507 (1993).

[4] H1 Collaboration, C. Kleinwort *et al.*, ICHEP-94 Glasgow, August (1994).
ZEUS Collaboration, M. Derrick *et al.*, DESY 95-013 (1995).
Also see the lectures of Wesley Smith in these proceedings.

[5] C. Peterson, D. Schlatter, I. Schmitt, and P. Zerwas, Phys. Rev. D **27**, 105 (1983).

[6] PYTHIA 5.6 and JETSET 7.3 *Physics Program and Manual*, CERN-TH.6488/92, and references: T. Sjöstrand, Computer Phys. Comm. **39**, 347 (1986); T. Sjöstrand and H. U.Bengtsson, Computer Phys. Comm. **43**, 367 (1987); H. U. Bengtsson and T. Sjöstrand, Computer Phys. Comm. **46**, 43 (1987).

[7] E687 Collaboration, P. L. Frabetti *et al.*, Phys. Lett. B **308**, 194 (1993).

[8] E687 Collaboration, P. L. Frabetti *et al.*, Phys. Lett. B **370**, 222 (1996).

[9] UCLA-Saclay Collaboration, S. Erhan *et al.*, Phys. Lett. B **85**, 447 (1979);
CERN-Bologna-Frascati Collaboration, M. Basile *et al.*, Lett. Nuovo Cimento **340**, 487 (1981).
E595 Collaboration, J. L. Ritchie *et al.*, Phys. Lett. B **138**, 213 (1984);
LEBC-EHS Collaboration, M. Aguilar-Benitez *et al.*, Z. Phys. C **31**, 489 (1986);
ACCMOR Collaboration, S. Barlag *et al.*, Z. Phys. C **49**, 555 (1991);
WA82 Collaboration, M. Adamovich *et al.*, Phys. Lett. B **305**, 402 (1993);
E769 Collaboration, G. A. Alves *et al.*, Phys. Rev. Lett. **72**, 812 (1994).

[10] E687 Collaboration, P. L. Frabetti *et al.*, Phys. Rev. Lett. **70**, 1381 (1993); Phys. Rev. Lett. **70**, 1775 (1993); Phys. Rev. Lett. **70**, 2058 (1993); Phys. Rev. Lett. **71**, 827 (1993); Phys. Lett. B **232**, 429 (1994); Phys. Lett B **357**, 678 (1995).

[11] V. Khoze and M. Shifman, Usp. Fiz. Nauk **140**, 3 (1983); Sov. J. Nucl. Phys. **41**, 120 (1985);
I. I. Bigi, N. G. Uraltsev, and A. Vainshtein, Phys. Lett. B **293**, 430 (1992); B **297**, 477 (1993);
B. Blok and M. Shifman, Nucl. Phys. B **399**, 441 (1993).

[12] I. I. Bigi, *Quo Vadis, Fascinum?* Workshop on the Tau/Charm Factory, Argonne, IL, June 21-23, 1995 (AIP Conference Proceedings 349), pp. 331-342.

[13] J. P. Cumalat, in *The Fermilab Meeting DPF92*, 10-14 November 1992, edited by Carl H. Albright, Peter H. Kasper, Rajendran Raja, and John Yoh (World Scientific Publishing Co.).

[14] Jeffrey D. Richman and Patrica R. Burchat to be published in Rev. Mod. Phys.

[15] WA75 Collaboration, S. Aoki *et al.*, Prog. Theor. Phys. **89**, 131.

[16] BES Collaboration, J. Z. Bai *et al.*, SLAC preprint no. SLAC-PUB-95-6746 (1995).

[17] CLEO Collaboration, D. Acosta *et al.*, Phys. Rev. D **49**, 5690 (1994).

[18] E653 Collaboration, K. Kodama *et al.*, Phys. Lett. B **382**, 299 (1996).

[19] See, for example, Anna Hasenfratz and Peter Hasenfratz, Ann. Ref. Nucl. Part. Sci **35**, 559-604 (1985).

[20] Gustavo Burdman and Joachim Kambor, http://xxx.lanl.gov/hep-ph/hep-ph/9602353.

[21] E687 Collaboration, P. L. Frabetti *et al.*, Phys. Lett. B **364**, 461 (1995).

[22] D. M. Schmidt, R. J. Morrison, and M. S. Witherell, Nucl. Instrum. Methods, A **328**, 547 (1993).

[23] CLEO Collaboration, A. Bean *et al.*, Phys. Lett. B **317**, 647 (1993).

[24] E687 Collaboration, P. L. Frabetti *et al.*, Phys. Lett. B **307**, 262 (1993).

[25] E687 Collaboration, P. L. Frabetti *et al.*, Phys. Lett. B **313**, 253 (1993); Phys. Lett. B **328**, 187 (1994).

[26] James N. Simone, *Semileptonic Decays: An Update Down Under*, plenary talk presented at Lattice '95 Melbourne, Australia, Fermilab-Conf-96.017-T.

[27] CLEO Collaboration, F. Butler *et al.*, Phys. Rev. D **52**, 2656 (1995).

[28] E687 Collaboration, P. L. Frabetti *et al.*, Phys. Lett. B **382**, 312 (1996).

[29] Mark III Collaboration, J. Adler *et al.*, Phys. Rev. Lett. **62**, 1821 (1989).

[30] D. Scorna and N. Isgur, Phys. Rev. D **62**, 2783 (1995);
V. Lubicz *et al.*, Phys. Lett. B **274**, 415 (1992);
S. Narison, Phys. Lett. B **377**, 163 (1994);
N. B. Debchuk *et al.*, INFN preprint INFN0ISS 95/18, (submitted to Sov. J. Nucl. Phys.).

[31] D. Scorna and N. Isgur, Phys. Rev. D **62**, 2783 (1995).

[32] J. G. Körner and M. Krämer, Phys. Lett. B **275**, 495 (1992).

[33] M. Bauer, B. Stech, and M. Wirbel, Z. Phys. C**29**, 637 (1985);
M. Bauer and M. Wirbel, Z. Phys. C **42**, 671 (1989).

[34] P. Frabetti *et al.*, Phys. Lett. B **321**, 295 (1994).

[35] M. Adamovich *et al.*, Phys. Lett.B **280**, 163 (1992).

[36] J. C. Anjos *et al.*, Phys. Rev. D **44**, R3371 (1991).

[37] J. Alexander *et al.*, Phys. Rev. Lett. B **65**, 1184 (1990).

[38] Thomas E. Browder, Klaus Honscheid, and Daniele Pedrini, to be submitted to Ann. Rev. Nucl. Part. Sci.

[39] P. Frabetti *et al.*, Phys. Lett. B **331**, 217 (1994).

[40] J. Adler *et al.*, Phys. Lett. B **196**, 107 (1987).

[41] J. C. Anjos *et al.*, Phys. Rev. D **48**, 56 (1993).

[42] H. Albrecht *et al.*, Phys. Lett. B **308**, 435 (1993).

[43] P. Frabetti *et al.*, Phys. Lett B **351**, 591 (1995).

[44] J. C. Anjos *et al.*, Phys. Rev. Lett. **62**, 125 (1989).

[45] Particle Data Group, R. M. Barnett *et al.*, Review of Particle Physics, Phys. Rev. D **54**, 557 (1996).

[46] P. Frabetti *et al.*, Phys. Lett. B **331**, 217 (1994).

[47] J. C. Anjos *et al.*, Phys. Rev. D **48**, 56 (1993).

[48] H. Albrecht *et al.*, Phys. Lett. B **308**, 435 (1993).

[49] E791 Collaboration, E. M. Aitala et al., Phys. Lett. B **371**, 157 (1996).

[50] R. Vogt and S. J. Brodsky, Nucl. Phys. B **438**, 261 (1996).